



Design and implementation of a robust and nonlinear flight control system for an unmanned helicopter

Guowei Cai^a, Ben M. Chen^{b,*}, Xiangxu Dong^b, Tong H. Lee^b

^a Temasek Laboratories, National University of Singapore, Singapore 117411, Singapore

^b Department of Electrical & Computer Engineering, National University of Singapore, Singapore 117576, Singapore

ARTICLE INFO

Article history:

Available online 4 March 2011

Keywords:

Unmanned aerial vehicles
Unmanned systems
Nonlinear flight dynamics
Flight control
Robust control

ABSTRACT

In this work, we focus on the design and implementation of a robust flight control system for an unmanned helicopter. A comprehensive nonlinear model for an unmanned helicopter system, which is built by our research team at the National University of Singapore, is first presented. A three-layer control architecture is then adopted to construct an automatic flight control system for the aircraft, which includes (1) an inner-loop controller designed using the H_∞ control technique to internally stabilize the aircraft and at the same time yield good robustness properties with respect to external disturbances, (2) a nonlinear outer-loop controller to effectively control the helicopter position and yaw angle in the overall flight envelope, and lastly, (3) a flight-scheduling layer for coordinating flight missions. Design specifications for military rotorcraft set for the US army aviation are utilized throughout the whole process to guarantee a top level performance. The result of actual flight tests shows our design is very successful. The unmanned helicopter system is capable of achieving the desired performance in accordance with the military standard under examination.

© 2011 Elsevier Ltd. All rights reserved.

1. Introduction

In recent years, research and development of unmanned vehicles have gained much attention in the academic and military communities worldwide. They are developed to be capable of working autonomously without interference of a human pilot. Challenge is that they need to deal with various situations arisen in much complicated and uncertain environments, such as unexpected obstacles, enemies attacking and device failures. Besides, they are required to communicate with technical personnel in the ground station. Consideration on a wide range of factors needs to be taken. Control systems are required to integrate both basic input–output control laws, and high-level functionalities such as decision making. Software systems for unmanned vehicles are required to perform multi-level tasks, such as from hardware driving to device operation management.

Among various unmanned aerial vehicles (UAVs), small-scale unmanned helicopters are an ideal platform for academic research. Besides having the characteristics of full-scale rotorcraft, it owns some unique and attractive features such as low cost, easy operation, and extreme agility. During the last two decades, many research groups have chosen such platforms for their research

purposes (see, e.g., [18,22,24]). Some commercial companies have also adopted them as the baseline to build their commercial UAV products for practical missions such as aerial photography and surveillance (see, for example, [12,25]).

Flight control system design is one of the core issues in the development of a fully functional unmanned rotorcraft. In the literature, there are a number of control techniques successfully implemented, which include the neural network approach [11], the differential geometry method [17], the robust and H_∞ control approach [13,15,28], the composite nonlinear feedback control with decoupling approach [21], and the model predictive approach [24] to name a few. However, many of the works reported focus merely on the basic autonomy. In other words, the control system design procedures are generally lack of evaluation using professional design specifications such as rotorcraft handling qualities.

The aim of this work is to design a robust flight control system for our small-scale UAV helicopter, HeLion (as shown in Fig. 1), to achieve the desired performance defined in ADS-33D-PRF [1] for military rotorcraft. To realize this goal, we first obtain a high-fidelity nonlinear flight dynamics model for HeLion, and then carry out to design a flight control system with three hierarchical layers, in which an inner-loop layer is for stabilizing the UAV helicopter, an outer-loop layer is for controlling its position and heading angle, and finally a flight-scheduling layer for coordinating flight missions. We would like to highlight that in our design formulation of the inner-loop controller, we formulate wind gusts as an

* Corresponding author. Tel.: +65 6516 2289; fax: +65 6779 1103.

E-mail addresses: tslaig@nus.edu.sg (G. Cai), bmchen@nus.edu.sg (B.M. Chen), dong07@nus.edu.sg (X. Dong), eleleeth@nus.edu.sg (T.H. Lee).

Nomenclature

Symbols used in flight dynamics model

A_{b_s}	coupling effect from b_s to a_s [s^{-1}]	S_{hf}	effective horizontal fin area [m^2]
A_{lon}	direct linkage gain from δ_{lon} to a_s [rad]	S_{vf}	effective vertical fin area [m^2]
a_s	longitudinal tip-path-plane (TPP) flapping angle [rad]	T	main rotor thrust [N]
B_B	translational transformation matrix from body frame to NED frame [NA]	T_{tr}	tail rotor thrust [N]
B_{a_s}	coupling effect from a_s to b_s [s^{-1}]	$V_a = (u_a, v_a, w_a)'$	velocity vector relative to the air in body frame [m/s]
B_{lat}	direct linkage gain from δ_{lat} to b_s [rad]	$V_b = (u, v, w)'$	velocity vector in body frame [m/s]
b_{mr}	main rotor blade number [NA]	$V_{wind} = (u_{wind}, v_{wind}, w_{wind})'$	wind gust velocity vector in the body frame [m/s]
b_s	lateral tip-path-plane (TPP) flapping angle [rad]	v_i	main rotor induced velocity [m/s]
b_{tr}	tail rotor blade number [NA]	$v_{i,tr}$	tail rotor induced velocity [m/s]
C_{D0}	drag coefficient of the main rotor blade [NA]	v_{vf}	local airspeed at the vertical fin [m/s]
$C_{l_{z,hf}}$	lift curve slope of the horizontal fin [rad^{-1}]	\hat{i}^2	intermediate variable in main rotor thrust calculation [m^2/s^2]
$C_{l_{z,mr}}$	lift curve slope of the main rotor blade [rad^{-1}]	\hat{i}_{tr}^2	intermediate variable in tail rotor thrust calculation [m^2/s^2]
$C_{l_{z,tr}}$	lift curve slope of the tail rotor blade [rad^{-1}]	w_{hf}	local vertical speed at the horizontal fin [m/s]
$C_{l_{z,vf}}$	lift curve slope of the vertical fin [rad^{-1}]	X_{mr}, Y_{mr}, Z_{mr}	aerodynamic forces generated by main rotor [N]
c_{mr}	main rotor blade chord length [m]	$X_{fus}, Y_{fus}, Z_{fus}$	aerodynamic forces generated by fuselage [N]
c_{tr}	tail rotor chord length [m]	Y_{tr}	aerodynamic force generated by tail rotor [N]
C_{lon}	linkage gain from δ_{lon} to longitudinal stabilizer-bar TPP flapping angle [rad]	Y_{vf}	aerodynamic force generated by vertical fin [N]
D_{hf}	horizontal fin's longitudinal position behind the center of gravity (CG) [m]	Z_{hf}	aerodynamic force generated by horizontal fin [N]
D_{lat}	linkage gain from δ_{lon} to lateral stabilizer-bar TPP flapping angle [rad]	δ_{col}	normalized collective pitch servo input (-1, 1) [NA]
D_{tr}	tail rotor hub's longitudinal position behind the CG [m]	δ_{lat}	normalized aileron servo input (-1, 1) [NA]
D_{vf}	vertical fin's longitudinal position behind the CG [m]	δ_{lon}	normalized elevator servo input (-1, 1) [NA]
F_g	gravity force vector [N]	δ_{ped}	normalized rudder servo input (-1, 1) [NA]
F_b	aerodynamic force vector [N]	$\delta_{ped,int}$	intermediate state in yaw rate gyro dynamics [rad]
H_{mr}	main rotor hub's vertical position above the CG [m]	δ_{ped}	collective pitch angle of the tail rotor blade [rad]
H_{tr}	tail rotor hub's vertical position above the CG [m]	$\theta_{col,0}$	trim offset of the main blade's collective pitch angle [rad]
H_{vf}	vertical fin's vertical position above the CG [m]	$\theta_{ped,0}$	trim offset of the tail blade's collective pitch angle [rad]
g	local acceleration of gravity in Singapore [m/s^2]	λ_{vf}	indicator of the vertical fin expose to tail rotor wake [NA]
$I = \text{diag}\{I_{xx}, I_{yy}, I_{zz}\}$	moment of inertia matrix in body frame [$kg\ m^2$]	ρ	air density [$kg\ m^{-3}$]
K_I	integral gain of embedded controller [NA]	τ_m	time constant of bare main rotor [s]
K_P	proportional gain of embedded controller [NA]	τ_s	time constant of stabilizer bar [s]
K_a	ratio of yaw rate to normalized rudder input [rad/s]	ϕ, θ, ψ	Euler angles [rad]
K_{col}	ratio of main rotor blade collective pitch to collective pitch servo input [rad]	Ω	main rotor rotating speed [rad/s]
K_{ped}	ratio of tail rotor blade collective pitch to rudder servo input [rad]	$\Omega_b = (p, q, r)'$	angular rate vector in body frame [rad/s]
K_{sb}	ratio of main rotor blade cyclic pitch to stabilizer-bar TPP tilting [NA]	Ω_{tr}	tail rotor rotating speed [rad/s]
K_β	main rotor spring constant [N m]	<i>Parameters for flight control system design</i>	
L_{mr}, M_{mr}, N_{mr}	aerodynamic moments generated by main rotor [$kg\ m^2$]	A	state matrix of the linearized inner-loop model
L_{vf}, N_{vf}	aerodynamic moments generated by vertical fin [$kg\ m^2$]	B	input matrix of the linearized inner-loop model
L_{tr}, N_{tr}	aerodynamic moments generated by tail rotor [$kg\ m^2$]	E	disturbance matrix of the linearized inner-loop model
M_b	aerodynamic moment vector [$kg\ m^2$]	F	feedback gain matrix of the inner-loop control law
M_{hf}	aerodynamic moment generated by horizontal fin [$kg\ m^2$]	G	tracking matrix of the inner-loop control law
m	helicopter mass [kg]	h_{in}	controlled output handling the constraints on input and partial state variables
P_c	climbing power of main rotor [W]	h_{out}	primary controlled output
P_i	induced power of main rotor [W]	k_ψ	feedback gain of outer-loop heading control
$P_n = (p_x, p_y, p_z)'$	position vector in north-east-down (NED) frame [m]	k_{att}	ratio of off- to on-axis attitude responses
P_{pa}	parasite power of main rotor [W]	k_{qik}	ratio of peak rate to peak angle
P_{pr}	profile power of main rotor [W]	t_{set}	settling time when the attitude response returns to 10% of the peak value
R	main blade radius [m]	u	input vector of the linearized model
R_{tr}	tail blade radius [m]	w	wind gust disturbance
S_B	rotational transformation matrix from body to NED frames [NA]	x	state vector of the linearized model
S_{fx}	effective longitudinal fuselage drag area [m^2]	y	measurement output vector of the linearized model
S_{fy}	effective lateral fuselage drag area [m^2]	y_{trim}	trimmed measurement output of the linearized model
S_{fz}	effective vertical fuselage drag area [m^2]	τ_p	phase delay of attitude response
		ω_{BW}	bandwidth of attitude response
		ω_{CF}	crossover frequency
		ω_{dst}	disturbance rejection bandwidth
		$[\cdot]_{CNF}$	parameters of the outer-loop CNF controller

external disturbance input to the UAV system. The H_∞ optimization technique is thus an ideal choice for attenuating such a disturbance and minimizing the effects of wind gusts to the overall system. We should note that our approach is rather different from those under the H_∞ control framework reported in the literature. For example, in Weilemann et al. [28], the H_∞ control technique is employed in two decoupled subsystems (one for the translational, pitch and roll motions, and the other for the heave and yaw motions) without experimental tests. Gadewadikar et al. [15] formulate the inner-loop control of an unmanned helicopter as a static measurement output feedback H_∞ control problem. Likewise, the design is presented without experimental verification on the actual platform. In Fujiwara et al. [13], an H_∞ automatic path tracking control law for a small-scale UAV helicopter is proposed and realized. It is, however, only utilized to control the horizontal velocity. As for the outer-loop layer, we adopt a newly developed composite nonlinear feedback (CNF) control technique to achieve a high performance position control. The CNF control consists of a linear feedback law and a nonlinear feedback law without any switching element. The linear feedback part is designed to yield a closed-loop system with a small damping ratio for a quick response, while at the same time not exceeding the actuator limits for the desired command input levels. The nonlinear feedback law is used to increase the damping ratio of the closed-loop system as the system output approaches the target reference to reduce the overshoot caused by the linear part. Finally,

we note that the nonlinear flight dynamics model is also utilized in the hardware-in-the-loop simulation process to stimulate more accurate features before the actual flight tests. We also note that a preliminary version of this work has been reported in [3].

The outline of this paper is as follows: Section 2 presents a comprehensive nonlinear flight dynamics model for the UAV helicopter system, whereas Section 3 provides a detailed description on the three-layer control system design procedure. The hardware-in-the-loop simulation and actual full-envelope flight test results are given in Section 4 together with the analysis and evaluation of the flight performance and reliability of the overall system using the standards set in [1]. Finally, we draw some concluding remarks in Section 5.

2. Flight dynamics modeling

An accurate flight dynamics model, which is based on the first-principles modeling approach, has been developed for our small-scale UAV helicopters. Besides the kinematics and rigid-body dynamics, two extra features, i.e., the stabilizer bar and factory-installed yaw rate gyro dynamics, are included. The proposed nonlinear model has fifteen states and four inputs, which are illustrated in Fig. 2 and summarized in Table 1. We note that the variable $\delta_{ped,int}$ in Table 1 is associated with a built-in controller in the yaw channel of the hobby helicopter. For ease of references, we list the physical meanings of all of the parameters at the beginning of this paper. Regarding the parameter identification, a five-step identification method, which includes (1) direct measurement, (2) ground test, (3) flight test, (4) theoretical calculation, and (5)



Fig. 1. HeLion, a small-scale UAV helicopter.

Table 1

Physical descriptions of the state and input variables of the helicopter dynamic model.

Variable	Physical description	Unit
p_x, p_y, p_z	Position vector along NED frame x -, y -, and z -axes	m
u, v, w	Velocity vector along body frame x -, y -, and z -axes	m/s
p, q, r	Roll, pitch, and yaw angular rates	rad/s
ϕ, θ, ψ	Euler angles	rad
a_s, b_s	Longitudinal and lateral tip-path-plane (TPP) flapping angle	rad
$\delta_{ped,int}$	Intermediate state in yaw rate gyro dynamics	NA
δ_{lat}	Normalized aileron servo input $(-1, 1)$	NA
δ_{lon}	Normalized elevator servo input $(-1, 1)$	NA
δ_{col}	Normalized collective pitch servo input $(-1, 1)$	NA
δ_{ped}	Normalized rudder servo input $(-1, 1)$	NA

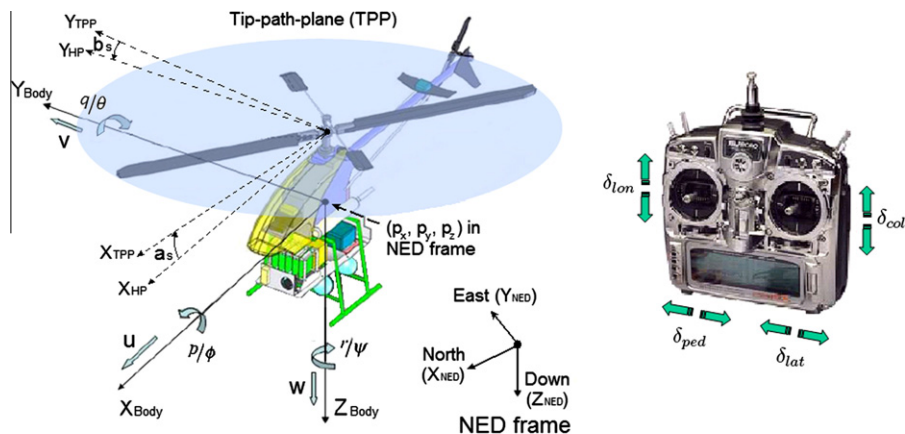


Fig. 2. Illustration for state and input variables.

empirical setting, has been developed and used to identify a complete dynamic model of our UAV helicopter. Interested readers are referred to [4] for the detailed information of the modeling structure and parameter identification procedure. In what follows, we have a brief overview of the nonlinear dynamical model obtained. We note that such a model is utilized to design a sophisticated flight control system in the next section and in the hardware-in-the-loop simulation process before conducting actual flight tests.

2.1. Kinematics

Two sets of kinematics equations are used to describe the relative motions between the two coordinate frames as shown in Fig. 2, i.e., the body frame and the north-east-down (NED) frame. The definitions on their origins and axes directions can be easily found in many texts.

The first set is for translational motion and given by

$$\dot{P}_n = B_B \cdot V_b \quad (1)$$

where $P_n = (p_x, p_y, p_z)$ is the position vector in the NED frame, $V_b = (u, v, w)$ is the velocity vector in the body frame, and B_B is the transformation matrix defined by

$$B_B = \begin{bmatrix} \mathbf{c}_\theta \mathbf{c}_\psi & \mathbf{s}_\theta \mathbf{s}_\theta \mathbf{c}_\psi & -\mathbf{c}_\theta \mathbf{s}_\psi & \mathbf{c}_\phi \mathbf{s}_\theta \mathbf{c}_\psi + \mathbf{s}_\phi \mathbf{s}_\psi \\ \mathbf{c}_\theta \mathbf{s}_\psi & \mathbf{s}_\theta \mathbf{s}_\theta \mathbf{s}_\psi + \mathbf{c}_\theta \mathbf{c}_\psi & \mathbf{c}_\phi \mathbf{s}_\theta \mathbf{s}_\psi - \mathbf{s}_\phi \mathbf{c}_\psi \\ -\mathbf{s}_\theta & \mathbf{s}_\phi \mathbf{c}_\theta & \mathbf{c}_\phi \mathbf{c}_\theta \end{bmatrix} \quad (2)$$

with $\mathbf{s}_{\star} = \sin(\star)$, $\mathbf{c}_{\star} = \cos(\star)$.

The second equation set is for the rotational motion and given as follows:

$$\begin{pmatrix} \dot{\phi} \\ \dot{\theta} \\ \dot{\psi} \end{pmatrix} = S_B \cdot \Omega_b \quad (3)$$

where $\Omega_n = (\phi, \theta, \psi)$ is the Euler angle vector, $\Omega_b = (p, q, r)$ is the angular rate vector in the body frame, and S_B is the corresponding transformation matrix defined by

$$S_B = \begin{bmatrix} 1 & \mathbf{t}_\theta \mathbf{s}_\phi & \mathbf{t}_\theta \mathbf{c}_\phi \\ 0 & \mathbf{c}_\phi & -\mathbf{s}_\phi \\ 0 & \mathbf{s}_\phi / \mathbf{c}_\theta & \mathbf{c}_\phi / \mathbf{c}_\theta \end{bmatrix} \quad (4)$$

with $\mathbf{t}_{\star} = \tan(\star)$.

It should be noted that although we do not use the wind frame in our modeling, we do, however, take the wind gust effect into account as follows:

$$V_a = V_b - V_{\text{wind}} \quad (5)$$

where $V_{\text{wind}} = (u_{\text{wind}}, v_{\text{wind}}, w_{\text{wind}})$ is the wind gust velocity vector, $V_a = (u_a, v_a, w_a)$ is the velocity vector relative to the air in the body frame.

2.2. Rigid-body dynamics

The six-degree-of-freedom (6-DOF) rigid-body dynamics of the UAV helicopter can be expressed by the following Newton–Euler equations:

$$\dot{V}_b = -\Omega_b \times V_b + \frac{F_b}{m} + \frac{F_g}{m} \quad (6)$$

and

$$\dot{\Omega}_b = I^{-1}(M_b - \Omega_b \times I \cdot \Omega_b) \quad (7)$$

where m is the total mass of the UAV helicopter, $F_g = (-mgs_\theta, mgs_\phi c_\theta, mgc_\phi c_\theta)$ is the gravity force vector expressed in the body frame, F_b is the aerodynamic force vector,

$I = \text{diag}\{I_{xx}, I_{yy}, I_{zz}\}$ is the moment of inertia matrix, and M_b is the aerodynamic moment vector. More specifically, F_b and M_b are respectively given by

$$F_b = \begin{pmatrix} F_{bx} \\ F_{by} \\ F_{bz} \end{pmatrix} = \begin{pmatrix} X_{mr} + X_{fus} \\ Y_{mr} + Y_{fus} + Y_{tr} + Y_{vf} \\ Z_{mr} + Z_{fus} + Z_{hf} \end{pmatrix} \quad (8)$$

and

$$M_b = \begin{pmatrix} M_{bx} \\ M_{by} \\ M_{bz} \end{pmatrix} = \begin{pmatrix} L_{mr} + L_{vf} + L_{tr} \\ M_{mr} + M_{hf} \\ N_{mr} + N_{vf} + N_{tr} \end{pmatrix} \quad (9)$$

Here $(\cdot)_{mr}$, $(\cdot)_{tr}$, $(\cdot)_{fus}$, $(\cdot)_{vf}$, and $(\cdot)_{hf}$ stand for the main rotor, tail rotor, fuselage, vertical fin and horizontal fin of the helicopter, respectively. Next, we categorize all of the force and moment components into the following five groups. It is noted that the expressions are mainly based on the results presented in [16] and partially modified to be suitable for the small-scale helicopters like HeLion.

1. *Main rotor forces and moments*: We first calculate the main rotor thrust T and the induced velocity v_i using the following iterative scheme

$$\left. \begin{aligned} T &= \frac{\rho \Omega R^2 C_{Lz, mr} b_{mr} c_{mr}}{4} [w_a + a_s u_a - b_s v_a + \frac{2}{3} \Omega R (K_{col} \delta_{col} + \theta_{col,0}) - v_i] \\ v_i^2 &= \sqrt{\left(\frac{v_a^2}{2}\right)^2 + \left(\frac{T}{2\rho\pi R^2}\right)^2} - \frac{v_a^2}{2} \\ \hat{v}^2 &= u_a^2 + v_a^2 + (w_a + a_s u_a - b_s v_a)(w_a + a_s u_a - b_s v_a - 2v_i) \end{aligned} \right\} \quad (10)$$

where \hat{v}^2 is an intermediate variable in main rotor thrust calculation. We need to highlight that for any flight condition, the iteration scheme starts with the associated trim values of T , v_i and \hat{v}^2 , and in our identification process, we let it run for 10 steps to ensure the convergence of the iterative procedure.

Then, we compute the forces and moments generated by the main rotor as follows:

$$\left. \begin{aligned} X_{mr} &= -T \sin(a_s) \\ Y_{mr} &= T \sin(b_s) \\ Z_{mr} &= -T \cos(a_s) \cos(b_s) \\ L_{mr} &= (K_\beta + TH_{mr}) \sin(b_s) \\ M_{mr} &= (K_\beta + TH_{mr}) \sin(a_s) \\ N_{mr} &= -(P_{pr} + P_i + P_{pa} + P_c) / \Omega \end{aligned} \right\} \quad (11)$$

where the power components, including (1) the profile power P_{pr} , (2) the induced power P_i , (3) the climbing power P_c , and (4) the parasite power P_{pa} , are calculated by

$$\left. \begin{aligned} P_{pr} &= \frac{\rho \Omega R^2 C_{D0} b_{mr} c_{mr}}{8} [(\Omega R)^2 + 4.6(u_a^2 + v_a^2)] \\ P_i &= T v_i \\ P_c &= \begin{cases} -mgw_a, & \text{if } |w_a| < 0 \\ 0, & \text{if } |w_a| \geq 0 \end{cases} \\ P_{pa} &= |X_{fus} u_a| + |Y_{fus} v_a| + |Z_{fus} (w_a - v_i)| \end{aligned} \right\} \quad (12)$$

Here X_{fus} , Y_{fus} and Z_{fus} are fuselage forces addressed later.

2. *Tail rotor force and moments*: Similar to the main rotor thrust T , the tail rotor thrust T_{tr} is computed iteratively as follows

$$\left. \begin{aligned} T_{tr} &= \frac{\rho \Omega_{tr} R_{tr}^2 C_{Lz, tr} b_{tr} c_{tr}}{4} [v_a - r D_{tr} + p H_{tr} + \frac{2}{3} \Omega_{tr} R_{tr} (K_{ped} \bar{\delta}_{ped} + \theta_{ped,0}) - v_{i, tr}] \\ v_{i, tr}^2 &= \sqrt{\left(\frac{v_a^2}{2}\right)^2 + \left(\frac{T_{tr}}{2\rho\pi R_{tr}^2}\right)^2} - \frac{v_a^2}{2} \\ \hat{v}_{tr}^2 &= (w_a + q D_{tr})^2 + u_a^2 + (v_a - r D_{tr} + p H_{tr})(v_a - r D_{tr} + p H_{tr} - 2v_{i, tr}) \end{aligned} \right\} \quad (13)$$

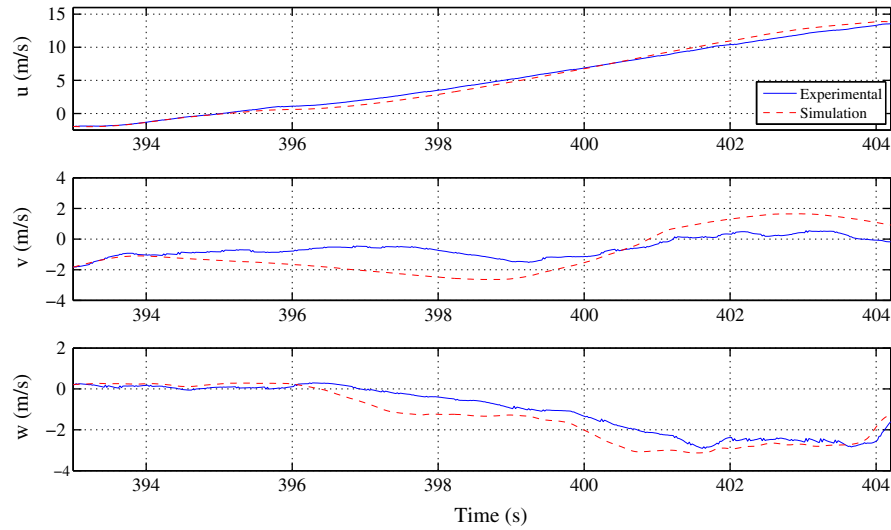
where $\bar{\delta}_{ped}$ is the collective pitch angle of the tail blade, which will be addressed later in Section 2.4. The initialization and

iteration-time setting are also similar to the counterparts adopted for the main rotor thrust. The tail rotor force and moments are then given by

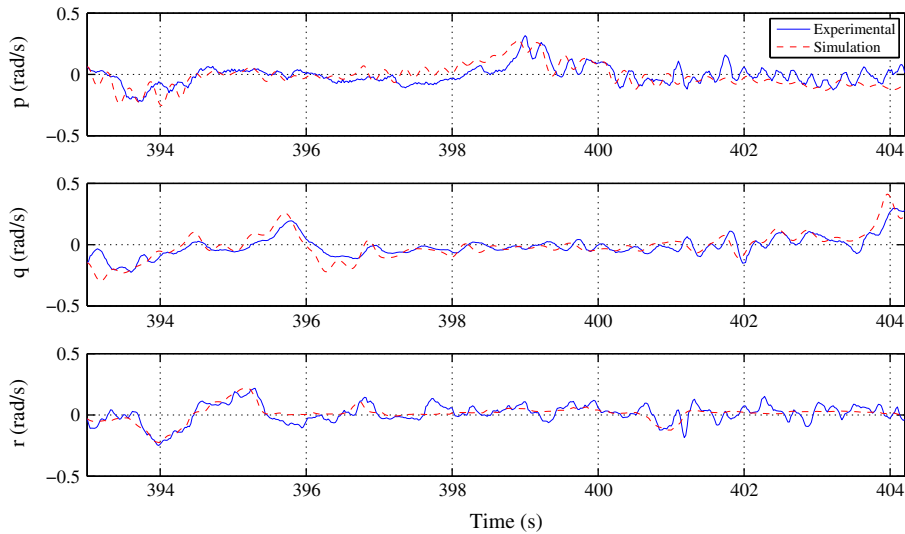
$$\left. \begin{aligned} Y_{tr} &= -T_{tr} \\ L_{tr} &= Y_{tr}H_{tr} \\ N_{tr} &= -Y_{tr}D_{tr} \end{aligned} \right\} \quad (14)$$

3. *Fuselage forces*: In fuselage forces computation, we need to consider the downwash effect caused by the main rotor. As such, the fuselage forces are expressed by

$$X_{fus} = \begin{cases} -\frac{\rho}{2}S_{fx}u_a v_i, & \text{if } |u_a| \leq v_i \\ -\frac{\rho}{2}S_{fx}u_a |u_a|, & \text{if } |u_a| > v_i \end{cases} \quad (15)$$



(a) Velocity response.



(b) Angular rate response.

Fig. 3. Nonlinear flight dynamics model validation—simulation vs. actual flight test.

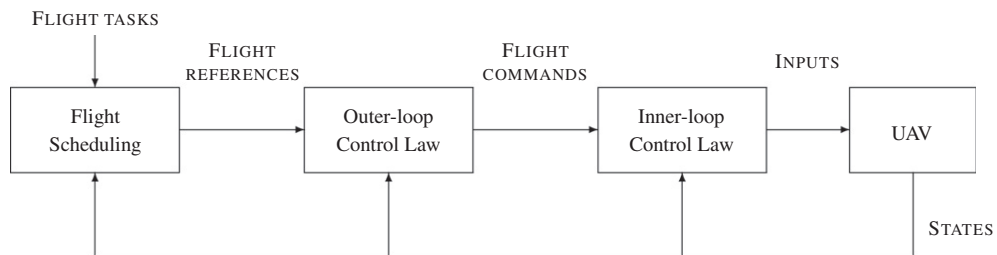


Fig. 4. Structure of the autonomous flight control system.

$$Y_{\text{fus}} = \begin{cases} -\frac{\rho}{2} S_{\text{fy}} v_a v_i, & \text{if } |v_a| \leq v_i \\ -\frac{\rho}{2} S_{\text{fy}} v_a |v_a|, & \text{if } |v_a| > v_i \end{cases} \quad (16)$$

$$Z_{\text{fus}} = -\frac{\rho}{2} S_{\text{fz}} (w_a - v_i) |w_a - v_i| \quad (17)$$

We note that the fuselage forces act on the CG of the helicopter and thus do not generate moments.

4. *Vertical fin force and moments*: For the vertical fin, we need to consider its stall effect and calculate the vertical fin force as

$$Y_{\text{vf}} = \begin{cases} -\frac{\rho}{2} C_{\text{L}\alpha, \text{vf}} S_{\text{vf}} v_{\text{vf}} |u_a|, & \text{if } |v_{\text{vf}}| \leq 0.3 |u_a| \\ -\frac{\rho}{2} S_{\text{vf}} v_{\text{vf}} |v_{\text{vf}}|, & \text{if } |v_{\text{vf}}| > 0.3 |u_a| \text{ (surface stalled)} \end{cases} \quad (18)$$

where $v_{\text{vf}} = v_a - rD_{\text{vf}} - \lambda_{\text{vf}} v_{\text{tr}}$ is the local lateral airspeed at the vertical fin. The factor λ_{vf} indicates whether the vertical fin is exposed to the tail rotor wake ($\lambda_{\text{vf}} = 1$ if the vertical fin is exposed to the tail rotor, otherwise $\lambda_{\text{vf}} = 0$).

The moments generated by the vertical fin force are given by

$$\left. \begin{aligned} L_{\text{vf}} &= Y_{\text{vf}} H_{\text{vf}} \\ N_{\text{vf}} &= -Y_{\text{vf}} D_{\text{vf}} \end{aligned} \right\} \quad (19)$$

5. *Horizontal fin force and moment*: For horizontal fin, both the stall effect and the main rotor wake are required to be taken into account. The resulting horizontal fin force is computed by

$$Z_{\text{hf}} = \begin{cases} -\frac{\rho}{2} C_{\text{L}\alpha, \text{hf}} S_{\text{hf}} w_{\text{hf}} |u_a|, & \text{if } |w_{\text{hf}}| \leq 0.3 |u_a| \\ -\frac{\rho}{2} S_{\text{hf}} w_{\text{hf}} |w_{\text{hf}}|, & \text{if } |w_{\text{hf}}| > 0.3 |u_a| \text{ (surface stalled)} \end{cases} \quad (20)$$

where $w_{\text{hf}} = w_a + q D_{\text{hf}} - v_i$ is the local vertical speed at the horizontal fin.

The horizontal fin moment is then computed by

$$M_{\text{hf}} = Z_{\text{hf}} H_{\text{hf}} \quad (21)$$

2.3. Main rotor flapping dynamics

The main rotor flapping dynamics is described by two coupled first-order differential equations:

$$\left. \begin{aligned} \dot{a}_s &= -\frac{(\tau_m + K_{\text{sb}} \tau_s)}{\tau_s} q - \frac{1}{\tau_s} a_s + \frac{\tau_m A_{\text{bs}}}{\tau_s} b_s + \frac{(A_{\text{lon}} + K_{\text{sb}} C_{\text{lon}})}{\tau_s} \delta_{\text{lon}} \\ \dot{b}_s &= -\frac{(\tau_m + K_{\text{sb}} \tau_s)}{\tau_s} p + \frac{\tau_m B_{\text{bs}}}{\tau_s} a_s - \frac{1}{\tau_s} b_s + \frac{(B_{\text{lat}} + K_{\text{sb}} D_{\text{lat}})}{\tau_s} \delta_{\text{lat}} \end{aligned} \right\} \quad (22)$$

The above flapping dynamics is derived particularly for RC-purpose helicopters equipped with the stabilizer bar. Interested readers are referred to [20] for the derivation process which focuses on the on-axis dynamics without considering the coupling effects, that is, the items containing A_{bs} and B_{as} .

2.4. Yaw rate gyro dynamics

Due to the over sensitivity of the yaw channel of hobby-based helicopters, a yaw rate gyro associated with an embedded controller is commonly equipped to facilitate the human pilot for heading-hold. This feature is still retained in our UAV system for the convenience of manual control. In [4], we have conducted a series of experimental tests and verified that the embedded controller is a PI control law. Based on the experimental result, we first define an intermediate state $\delta_{\text{ped, int}}$, which is the integration of the error between the yaw channel input signal and the yaw rate feedback, and then express the yaw rate gyro dynamics as

$$\left. \begin{aligned} \dot{\delta}_{\text{ped, int}} &= K_a \delta_{\text{ped}} - r \\ \ddot{\delta}_{\text{ped}} &= K_p \dot{\delta}_{\text{ped, int}} + K_i \delta_{\text{ped, int}} \end{aligned} \right\} \quad (23)$$

where K_p and K_i are respectively the proportional and integral gains for the embedded controller, K_a is for the normalization of the rudder input, δ_{ped} , which is determined via a constant-rate hovering-turn experiment by calculating the ratio of yaw rate r to δ_{ped} . Lastly, $\ddot{\delta}_{\text{ped}}$ is used to calculate the tail rotor thrust, T_{tr} .

Finally, we combine (1)–(23) to provide a 15th order nonlinear dynamical model. We have implemented the previously mentioned five-step identification procedure to identify all the physical parameters for HeLion. The more detailed results are summarized in a supplementary document [2] for easy references. To demonstrate the accuracy of the identified model, we show in Fig. 3 a verification result, in which the response of the obtained model is compared to that of a manual flight with the forward speed ranging from 0 (hover) to 14 m/s (high speed flight). Note that the simulation result is obtained using the input signals recorded in the manual flight. It clearly indicates that the obtained model is able to effectively capture the dynamics of HeLion in a fairly wide flight envelope.

3. Robust flight control system design

We carry out in this section the design of a robust flight control system for our UAV helicopter. As mentioned earlier, a three-layer flight control structure is adopted. Its schematic diagram is depicted in Fig. 4, in which (1) the inner-loop control law implements H_∞ control technique to internally stabilize the UAV helicopter and to achieve a good wind gust attenuation, (2) the outer-loop law is designed using the CNF control technique to yield a good performance in positioning and heading, and (3) the flight-scheduling layer generates the desired flight trajectories.

3.1. Inner-loop control law design

The inner-loop control law is designed based on the H_∞ control technique. Lightness in weight and smallness in size are two sides of the coin for small-scale UAV helicopters. The small-scale UAV helicopters possess more agility and maneuverability, but they are more vulnerable to the environmental disturbances such as wind gusts. As such, the H_∞ control method, a technique developed to attenuating external disturbances while maintaining the closed-loop stability, is a natural choice for the inner control loop to realize both internal stabilization and disturbance rejection. In general, the design procedure consists of four steps, i.e., (1) dynamic model linearization, (2) specification selection, (3) flight control law design, and (4) performance evaluation. As we aim to develop an automatic flight control system that is applicable for a wide flight envelope, we need to design a series of inner control laws for various critical flight conditions (for HeLion, we choose the flight conditions with forward speeds $u = 00, 3, 6, 9,$ and 12 m/s, respectively). The control laws are then implemented through a gain scheduling scheme for realizing full envelope flights.

3.1.1. Linearization of the nonlinear dynamical model

In order to apply the H_∞ control technique to design an inner-loop control law for our UAV helicopter, we need to first linearize the nonlinear dynamical model of the unmanned system obtained in the previous section. The linearized models can be described as

$$\begin{pmatrix} \dot{p}_n \\ \dot{\psi} \end{pmatrix} = \begin{bmatrix} B_B & 0 \\ 0 & 1 \end{bmatrix} \begin{pmatrix} V_b \\ r \end{pmatrix} \quad (24)$$

and

$$\dot{\mathbf{x}} = \mathbf{A}\mathbf{x} + \mathbf{B}\mathbf{u} \quad (25)$$

where the state vector $\mathbf{x} = \mathbf{x}_{\text{act}} - \mathbf{x}_{\text{trim}}$ is the difference between the actual state variables and their trimmed values. Similarly, the input

vector $\mathbf{u} = \mathbf{u}_{act} - \mathbf{u}_{trim}$ is the difference between the actual input variables and their trimmed values. More specifically, \mathbf{u}_{act} and \mathbf{x}_{act} are respectively defined as

$$\mathbf{u}_{act} = (\delta_{lat} \quad \delta_{lon} \quad \delta_{col} \quad \delta'_{ped}) \quad (26)$$

and

$$\mathbf{x}_{act} = (u \quad v \quad p \quad q \quad \phi \quad \theta \quad a_s \quad b_s \quad w \quad r \quad \delta'_{ped,int}) \quad (27)$$

For the hovering flight condition, the trim values of the state and input variables are respectively listed in Tables 2 and 3. The state and input matrices A and B of the corresponding linearized model are given by

$$A = \begin{bmatrix} -0.0335 & 0 & 0 & 0 & 0 & -9.7810 & -9.9253 & 0 & 0.0006 & 0 & 0 \\ 0 & -0.3201 & -0.0045 & 0 & 9.7737 & -0.0003 & 0 & 9.9252 & 0.0035 & 1.7068 & -8.8776 \\ 0 & -0.1416 & -0.0243 & 0 & 0 & 0 & 0 & 478.2872 & 0.0366 & 9.2300 & -48.0092 \\ 0 & -0.0002 & 0 & -0.0578 & 0 & 0 & 216.8400 & 0 & -0.0275 & 0 & 0 \\ 0 & 0 & 1 & 0.0000 & 0 & 0 & 0 & 0 & 0 & 0.0008 & 0 \\ 0 & 0 & 0 & 0.9993 & 0 & 0 & 0 & 0 & 0 & -0.0387 & 0 \\ 0 & 0 & 0 & -1.2301 & 0 & 0 & -4.0881 & 2.8000 & 0 & 0 & 0 \\ 0 & 0 & -1.2301 & 0 & 0 & 0 & 2.8120 & -4.0881 & 0 & 0 & 0 \\ 0.0005 & 0.0033 & 0 & -0.0054 & -0.3784 & -0.0079 & -0.0079 & 0.0478 & -0.7374 & 0 & 0 \\ 0.0005 & 0.3386 & 0.0577 & 0 & 0 & 0 & 0 & 0 & -0.3360 & -21.8848 & 113.8318 \\ 0 & 0 & 0 & 0 & 0 & 0 & 0 & 0 & 0 & -1 & 0 \end{bmatrix}$$

$$B = \begin{bmatrix} 0 & 0 & -0.0170 & 0 \\ 0 & 0 & -0.1032 & 6.4668 \\ 0 & 0 & -1.0930 & 34.9720 \\ 0 & 0 & -0.3275 & 0 \\ 0 & 0 & 0 & 0 \\ 0 & 0 & 0 & 0 \\ 0 & 3.1478 & 0 & 0 \\ 3.1478 & 0 & 0 & 0 \\ 0 & 0 & 21.0746 & 0 \\ 0 & 0 & 10.2735 & -82.9200 \\ 0 & 0 & 0 & -3.8500 \end{bmatrix}$$

Interested readers are referred to [2] for more detailed results for the other flight conditions.

3.1.2. Selection of design specifications

We follow the guideline given in [27] to select a series of design specifications to guarantee good performance in various categories, such as handling qualities, disturbance rejection, stability, and control usage. These specifications are originally defined in the military rotorcraft standards (see, for example, ADS-33D-PRF [1] and

Table 2
Trim values of the state variables for the hovering flight condition.

u	v	p	q	ϕ	θ	a_s	b_s	w	r	$\delta'_{ped,int}$
0	0	0	0	0.0387	0.0008	-0.0008	0.0048	0	0	0

Table 3
Trim values of the input variables for the hovering flight condition.

δ_{lat}	δ_{lon}	δ_{col}	δ_{ped}
0.0070	-0.0053	-0.1746	0

SAE-AS94900 [23]). For the hovering flight condition, the design specifications are selected as follows:

1. *Locations of eigenvalues:* All of the eigenvalues are required to be located at the left-half-plane to guarantee the system stability.
2. *Bandwidth of pitch and roll attitude responses:* This specification has requirements on both bandwidth ω_{BW} and phase delay τ_p , which are defined by

$$\left. \begin{aligned} \omega_{BW} &= \min(\omega_{BW,gain}, \omega_{BW,phase}) \\ \tau_p &= \frac{\Delta\Phi_{2\omega_{180}}}{57.3(2\omega_{180})} \end{aligned} \right\} \quad (28)$$

where ω_{180} is the frequency point where the phase crosses 180°; $\omega_{BW,gain}$ is the lowest frequency point where the corresponding gain is 6 dB larger than ω_{180} gain value; $\omega_{BW,phase}$ is the lowest frequency where the phase crosses 135°; and $\Delta\Phi_{2\omega_{180}}$ is the phase difference between ω_{180} and $2\omega_{180}$.

3. *Coupling effect between roll and pitch responses:* For this specification, step input signal is injected in δ_{lat} (or δ_{lon}). The resulting off- and on-axis attitude responses are compared. An upper limitation is set for k_{att} , the ratio of the off- to on-axis peak attitudes during the transient period.
4. *Coupling effect from heave control to yaw response:* This specification examines the 3-s yaw rate response due to a step input in heave direction. According to [1], the helicopter is required to achieve the new trimmed condition within 3 s. With this prerequisite, this specification sets the requirements for: (1) $k_{yaw,1}$, the ratio of the difference between peak yaw rate and yaw rate at 3 s to the heave velocity at 3 s, and (2) $k_{yaw,2}$, the ratio of peak yaw rate to the heave velocity at 3 s.
5. *Crossover frequency:* The crossover frequency (ω_{CF}) is defined as the frequency where the magnitude curve crosses 0 dB [10]. Following [10], broken points are set at the input channels δ_{lat} and δ_{lon} , and the frequency response of the resulting broken-loop input and output is examined. An upper limitation for the crossover frequency is set in this specification.
6. *Disturbance rejection bandwidth for attitude control:* The disturbance rejection bandwidth, ω_{dst} , is defined as the lowest frequency where the magnitude curve of attitude response to disturbance crosses -3 dB [10]. The attitude disturbance signal is required to be added to the bare attitude output generated by the helicopter dynamics. The main purpose of this specification is to evaluate the hold capability of the system in the presence of attitude disturbance [10].
7. *Quickness of pitch, roll, and yaw responses:* For each of the three cases, spike signal is adopted as the input. The ratio of peak rate to the corresponding peak angle, k_{qik} , measuring the quickness

of the response, is required to be larger than the defined lower limitation, which varies with respect to the minimum angle response.

8. *Attitude hold for spike disturbance input:* This specification evaluates the time-domain attitude hold capacity for the short-period spike input. Upper limitation is provided for the settling time, t_{set} , when the attitude response returns to within 10% of the peak attitude response.

Among them, the first specification is for the stability and is necessary for any control system. The performance in term of the remaining 7 specifications can be categorized into three performance levels with Level 1 being the best. In our design, we aim to achieve top level performance in all categories as set in [1]. The detailed specifications for the Level 1 requirements are to be given later together with the performance evaluation of our design.

3.1.3. *Controller design using H_∞ optimization technique*

Given a generalized system with a control input and an external disturbance input as well as a measurement output and a controlled output, the H_∞ control technique is to design a proper measurement feedback control law such that when it is applied to the given system, the worst case L_2 -gain between the controlled output and the disturbance input in the closed-loop system is

minimized. The design of the H_∞ inner-loop control law consists of three steps, i.e., (i) the problem formulation, (ii) the state-feedback H_∞ control law design, and (iii) the reduced-order observer design.

1. *Problem formulation:* We first formulate the inner-loop controller design into the framework of an H_∞ control problem. Considering a wind gust disturbance $\mathbf{w} = V_{wind} = (u_{wind}, v_{wind}, w_{wind})'$ effecting the UAV velocities in the x-, y- and z-directions, respectively, the linearized model of (25) can then be expressed as

$$\dot{\mathbf{x}} = \mathbf{A}\mathbf{x} + \mathbf{B}\mathbf{u} + \mathbf{E}\mathbf{w} \tag{29}$$

where the disturbance matrix $E = A E_{dst}$ with

$$E_{dst} = \begin{bmatrix} 1 & 0 & 0 \\ 0 & 1 & 0 \\ 0 & 0 & 0 \\ 0 & 0 & 0 \\ 0 & 0 & 0 \\ 0 & 0 & 0 \\ 0 & 0 & 0 \\ 0 & 0 & 1 \\ 0 & 0 & 0 \\ 0 & 0 & 0 \end{bmatrix}$$

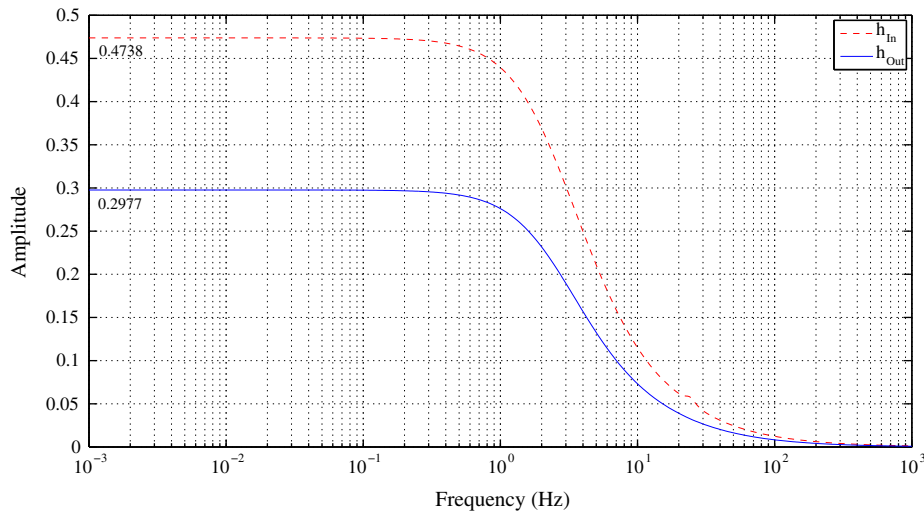


Fig. 5. Maximum singular values of the closed-loop transfer matrices in the hovering flight condition.

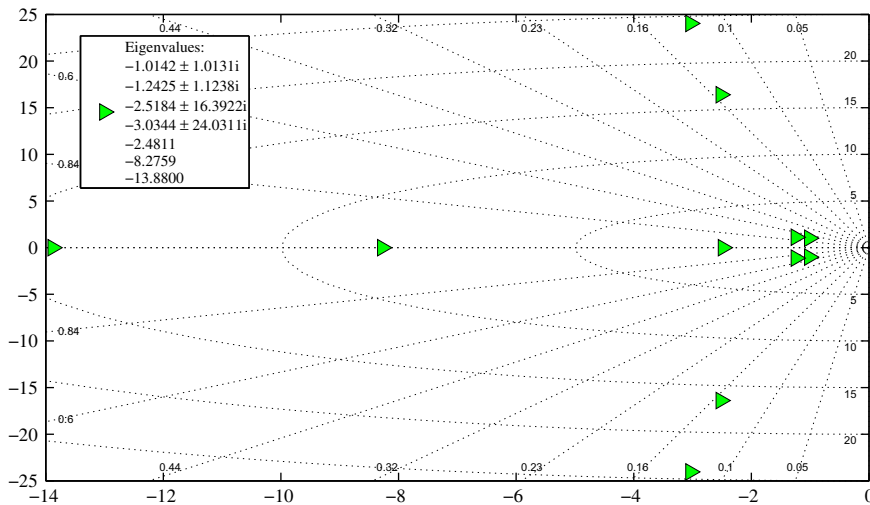


Fig. 6. Eigenvalues of the closed-loop system in the hovering flight condition.

The measurement output is given by

$$\mathbf{y} = (u \ v \ p \ q \ \phi \ \theta \ w \ r') - \mathbf{y}_{\text{trim}} := C_1 \mathbf{x} \quad (30)$$

where \mathbf{y}_{trim} is the trim value of the corresponding measurable state variables, and C_1 can be defined in an obvious fashion. As mentioned earlier, our primary task is to design a control law to internally stabilize the plant, and at the same time to yield

a good response of the state variables that are directly related and linked to the outer loop, i.e., u, v, w and r . Thus, the primary output to be controlled is selected as

$$\mathbf{h}_{\text{out}} := (u \ v \ w \ r') - \mathbf{h}_{\text{out,trim}} := C_{\text{out}} \mathbf{x} \quad (31)$$

where $\mathbf{h}_{\text{out,trim}}$ is the trim value of the corresponding \mathbf{h}_{out} , and C_{out} is the corresponding constant matrix. In order to handle

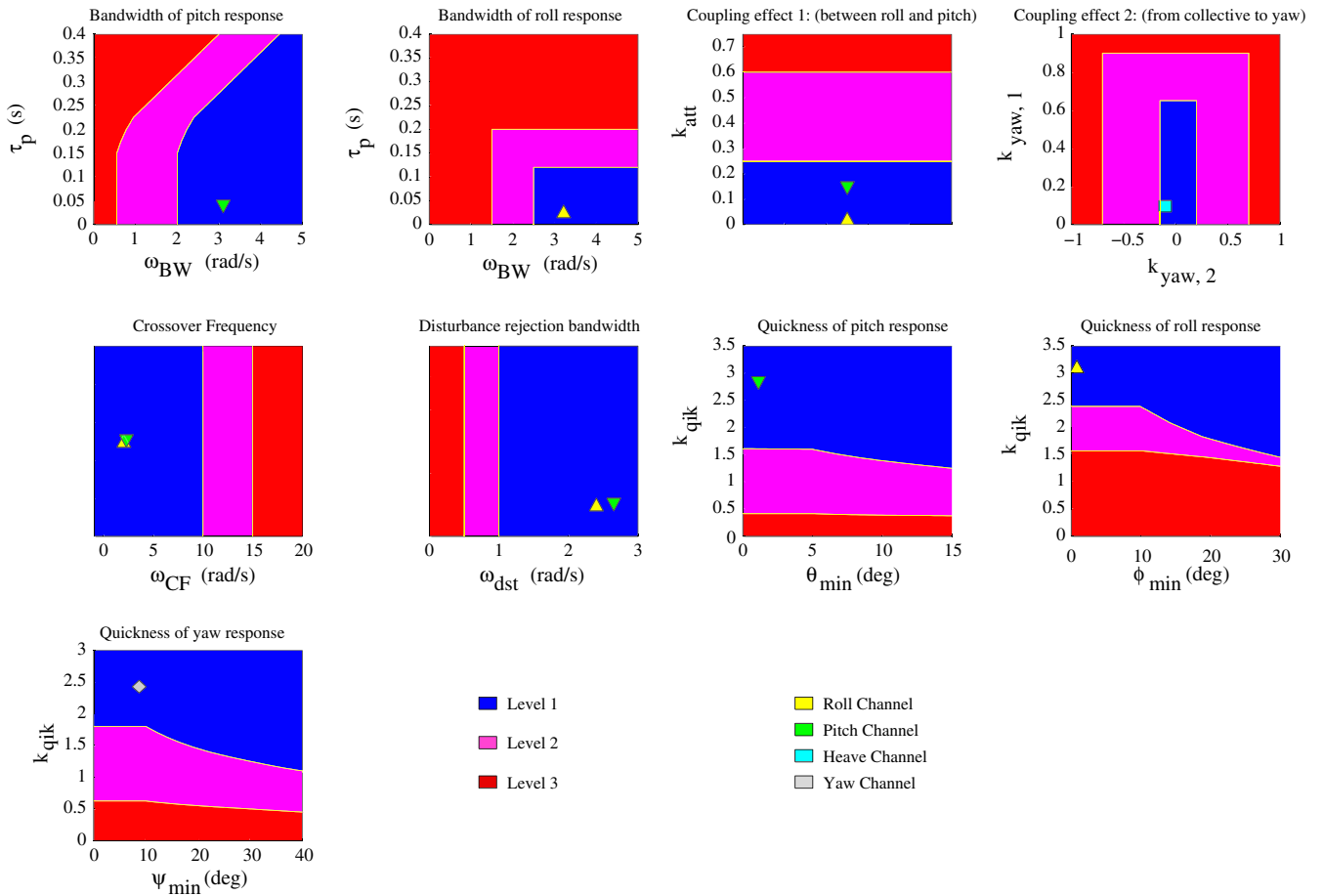


Fig. 7. Summarization of evaluation results for the hovering condition.

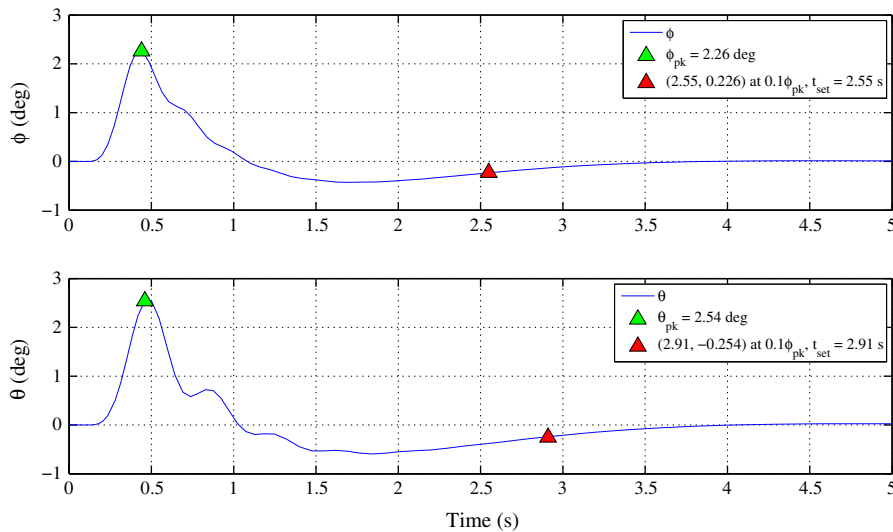


Fig. 8. Attitude hold examination for spike disturbance input.

the input constraints and constraints on other state variables, we adopt the following controlled output in the design process,

$$\mathbf{h}_{in} = C_2 \mathbf{x} + D_2 \mathbf{u} \tag{32}$$

with

$$C_2 = \begin{bmatrix} \mathbf{0}_{4 \times 11} \\ b_1 & 0 & 0 & 0 & 0 & 0 & 0 & 0 & 0 & 0 & 0 & 0 \\ 0 & b_2 & 0 & 0 & 0 & 0 & 0 & 0 & 0 & 0 & 0 & 0 \\ 0 & 0 & b_3 & 0 & 0 & 0 & 0 & 0 & 0 & 0 & 0 & 0 \\ 0 & 0 & 0 & b_4 & 0 & 0 & 0 & 0 & 0 & 0 & 0 & 0 \\ 0 & 0 & 0 & 0 & 0 & 0 & 0 & 0 & b_5 & 0 & 0 & 0 \\ 0 & 0 & 0 & 0 & 0 & 0 & 0 & 0 & 0 & b_6 & 0 & 0 \end{bmatrix}$$

and

$$D_2 = \begin{bmatrix} a_1 & 0 & 0 & 0 \\ 0 & a_2 & 0 & 0 \\ 0 & 0 & a_3 & 0 \\ 0 & 0 & 0 & a_4 \\ \mathbf{0}_{6 \times 4} \end{bmatrix}$$

where a_i 's and b_i 's are weighting parameters to be determined later. We note that under such a problem formulation, one can utilize the well studied H_∞ control theory (see, e.g., [6]) to design a measurement feedback control law (either a full order or reduced order) that would minimize the effect of the wind gust disturbance, i.e., to minimize the H_∞ norm of the closed-loop transfer matrix from the disturbance \mathbf{w} to the controlled output \mathbf{h}_{in} or \mathbf{h}_{out} or both. We note that physically the H_∞ norms of the closed-loop systems from \mathbf{w} to \mathbf{h}_{in} , say $T_{in}(s)$, and to \mathbf{h}_{out} , say $T_{out}(s)$, are representing the worst case L_2 -gains between the controlled output signals and the input wind gust disturbance, i.e.,

$$\|T_{in}\|_\infty = \sup_{\omega \in [0, \infty)} \sigma_{\max}[T_{in}(j\omega)] = \sup_{\|\mathbf{w}\|_2=1} \frac{\|\mathbf{h}_{in}\|_2}{\|\mathbf{w}\|_2}$$

and

$$\|T_{out}\|_\infty = \sup_{\omega \in [0, \infty)} \sigma_{\max}[T_{out}(j\omega)] = \sup_{\|\mathbf{w}\|_2=1} \frac{\|\mathbf{h}_{out}\|_2}{\|\mathbf{w}\|_2}$$

respectively, where $\sigma_{\max}[\cdot]$ denotes the maximal singular value of the matrix. It can be verified that the subsystem characterized by

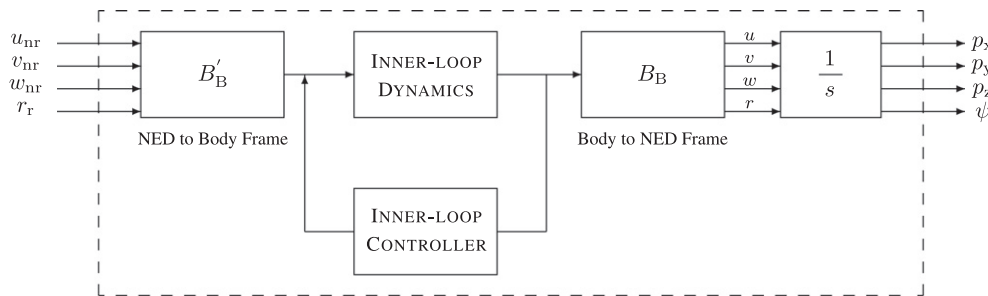


Fig. 9. Block diagram of the outer-loop dynamics with the inner-loop controller.

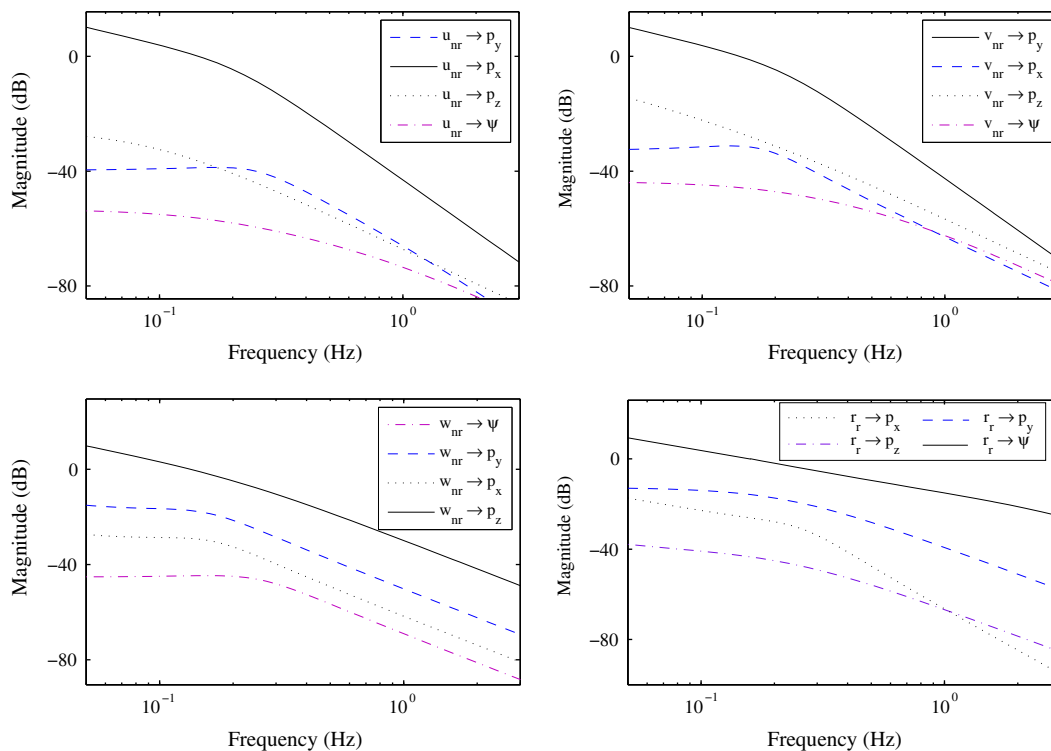


Fig. 10. Frequency-domain responses of the open outer loop.

the matrix triple (A, E, C_1) is left invertible and of minimum phase. It follows, for example, Chen [6], that the H_∞ optimization performance of the problem with measurement feedback is equivalent to that of the problem with state feedback.

2. *State-feedback H_∞ control law design*: Based on the above problem formulation and analysis, we follow the design procedure given in [6] to complete the state-feedback control law design.
 - (a) First, we determine the weighting parameters a_i 's for D_2 and b_i 's for C_2 , respectively. Once these parameters are fixed, we compute γ_{in}^* , which is the optimal H_∞ performance for the closed-loop system from the disturbance input \mathbf{w} to the controlled output \mathbf{h}_{in} over all the possible internally stabilizing controllers.
 - (b) It can be verified that matrix D_2 is of full column rank and the matrix quadruple (A, B, C_2, D_2) is left invertible and is free of invariant zeros. Thus, for any given $\gamma > \gamma_{in}^*$, its corresponding H_∞ γ -suboptimal state feedback law can be obtained as follows:

$$F = \begin{bmatrix} 0.0047 & -0.0869 & -0.0153 & -0.0013 & -0.8736 & -0.0342 & -0.1838 & -1.8391 & 0.0022 & -0.0238 & 0.0661 \\ 0.0806 & 0.0061 & 0.0113 & -0.0232 & 0.0775 & -0.8062 & -1.3922 & -0.0504 & -0.0009 & 0.0030 & 0.0162 \\ -0.0003 & -0.0057 & -0.0006 & -0.0001 & -0.0126 & 0.0011 & -0.0002 & -0.0492 & -0.0825 & -0.0021 & 0.0035 \\ 0.0007 & -0.0014 & -0.0039 & -0.0000 & -0.0087 & -0.0073 & 0.0144 & 0.0348 & -0.0000 & 0.0019 & 0.0134 \end{bmatrix}$$

$$\mathbf{u} = \mathbf{F}\mathbf{x} + \mathbf{G}\mathbf{r} = -(D_2' D_2)^{-1} (D_2' C_2 + B' P) \mathbf{x} + \mathbf{G}\mathbf{r} \quad (33)$$

where $\mathbf{r} = (V_{b,r}, r_r)' = (u_r, v_r, w_r, r_r)'$ is the reference signal vector generated by the outer-loop control law, P is the positive semi-definite stabilizing solution of the following H_∞ algebraic Riccati equation

$$A'P + PA + C_2' C_2 + PEE'P/\gamma^2 - (PB + C_2' D_2)(D_2' D_2)^{-1} (D_2' C_2 + B' P) = 0 \quad (34)$$

and the reference feedforward matrix G is given by

$$G = -[C_{out}(A + BF)^{-1} B]^{-1} \quad (35)$$

For a specified flight condition, we need to carefully select the weighting parameters. Three primary rules include: (1) all the design specifications mentioned earlier are required to be achieved, (2) the resulting inner-loop control law is physically realizable (see, for example, drastic closed-loop attitude response is prohibited), and (3) the physical limitations and constrains of miniature UAV helicopters (see, for example, the velocity response is slower than that of the attitude) should be considered. For the initial values of the weighting parameters, we choose a set that slightly changes

the poles' location of the system given in (25). Based on it, we gradually adjust the weighting parameters to meet the selected design specifications. After every change, we examine the above mentioned second and third rules to ensure that they are still intact. The tuning procedure is conducted iteratively until all the three primary rules are achieved. Taking HeLion's hovering condition as an example, after few trials, we obtain the final selection for the weighting parameters as

$$a_1 = 13, \quad a_2 = 12, \quad a_3 = 15, \quad a_4 = 30$$

$$b_1 = 1, \quad b_2 = 1.2, \quad b_3 = 1, \quad b_4 = 1, \quad b_5 = 1, \quad b_6 = 1$$

and the corresponding $\gamma_{in}^* = 0.4647$. We then select $\gamma = 0.48$ such that the resulting controller is implementable subject to the physical constrains of the helicopter system. We obtain the following γ -suboptimal controller gain matrices,

and

$$G = \begin{bmatrix} -0.0048 & 0.1133 & -0.0025 & 0.0237 \\ -0.0834 & -0.0084 & 0.0013 & 0.0128 \\ 0.0003 & 0.0065 & 0.1175 & 0.0021 \\ -0.0007 & 0.0017 & 0.0000 & -0.2617 \end{bmatrix}$$

3. *Reduced-order observer design*: Since three variables in the state vector, i.e., a_s , b_s and $\delta_{ped,int}$, are not measurable, we need to design a proper reduced-order observer for these variables in order to implement the state feedback law obtained in the previous step. The following reduced-order estimator will be used for all flight conditions under examination:

$$\dot{\mathbf{x}}_{in,cmp} = A_{in,cmp} \mathbf{x}_{in,cmp} + B_{in,cmp} \mathbf{y} + H_{in,cmp} \mathbf{u} \quad (36)$$

where

$$A_{in,cmp} = \begin{bmatrix} -10 & 0 & 0 \\ 0 & -10 & 0 \\ 0 & 0 & -12 \end{bmatrix}, \quad H_{in,cmp} = \begin{bmatrix} 0.2026 & 2.5729 & -0.0050 & -0.0000 \\ 2.5729 & -0.0663 & -0.0419 & -0.0000 \\ 0 & 0 & -1.0786 & 4.8913 \end{bmatrix}$$

Table 4

Selected mission task elements for full-envelope flight test.

MTE	Description
Forward speed test (25 s)	Start from hovering condition, accelerate to the predefined maximum speed (12 m/s) in 8 s, maintain the most efficient speed for 9 s, then decelerate to hover in 8 s
Stable hover (40 s)	Maintain hovering status at a designated point for 40 s, and keep the 3D position and heading angle unchanged
Backward speed test (33 s)	Start from hovering condition, accelerate to the predefined maximum speed (−4 m/s) in 4 s, maintain the most efficient speed for 25 s, then decelerate to hover in 4 s
Hovering turn (15 s)	Complete a 270-degree turning within 15 s, maintain the yaw rate of 18°/s, and keep the 3D position unchanged
Heave response (10 s)	Start from hovering condition, ascend to the designated point with 5 m higher, hover 2 s, then descend to original hovering position
Lateral reposition (18 s)	Start from hovering condition, accelerate to the predefined maximum lateral speed (5.5 m/s) in 9 s, then decelerate to hover at the designated point in 9 s
Turn to target (5 s)	Complete a fast 180-degree turning within 5 s, maintain the yaw rate of 36°/s, and keep the 3D position unchanged.
Slalom (38 s)	Start from hovering condition, accelerate to 6 m/s in 10 s, complete the predefined slalom maneuver in the following 18 s, and decelerate to hover in 10 s
Pirouette (25 s)	Complete a horizontal circle path with 10 m radius, keep the nose pointing to the center of the circle

$$B_{\text{in,cmp}} = \begin{bmatrix} 0.0093 & 0.0007 & -0.0381 & -1.2488 & 0.0007 & -0.0092 & 0.0014 & -0.0199 \\ 0.0034 & 0.0021 & -1.1142 & -0.0915 & 0.0021 & -0.0034 & 0.0018 & -0.0597 \\ -0.0001 & 0.0491 & -0.0076 & 0.0000 & 0.0708 & -0.0000 & 0.0352 & 0.0480 \end{bmatrix}$$

and

$$\begin{pmatrix} \hat{a}_s \\ \hat{b}_s \\ \hat{\delta}_{\text{ped,int}} \end{pmatrix} = \mathbf{x}_{\text{in,cmp}} + K_{\text{in,cmp}} \mathbf{y} \quad (37)$$

where

$$K_{\text{in,cmp}} = 10^{-3} \times \begin{bmatrix} -0.9378 & -0.0728 & 3.8102 & 25.0652 & 0 & 0 & -0.0003 & 1.9932 \\ -0.3448 & -0.2182 & 11.4164 & 9.2163 & 0 & 0 & 0.0009 & 5.9722 \\ 0 & -7.2439 & 0.1232 & 0 & 0 & 0 & 0.0046 & 104.9184 \end{bmatrix}$$

3.1.4. Performance evaluation

In this section, we carry out a comprehensive performance evaluation on the above H_∞ inner-loop control law. *Conduit* toolkit [26,27], a software package developed by the NASA Ames Research Center for assisting the flight control law design of military rotorcraft and aircraft, has been adopted for the straightforward graphical display of the selected design specifications (as shown in Fig. 7). Described below are the evaluation results for the hovering flight condition of HeLion.

1. *Singular values of the resulting closed-loop systems*: Although the controlled output \mathbf{h}_{in} is used in the control law design, the disturbance rejection capacity of the controlled output \mathbf{h}_{out} is practically more important as it is directly related to the position and yaw rate of the unmanned system. As such, we evaluate the frequency domain responses of the closed-loop transfer matrix from \mathbf{w} to \mathbf{h}_{in} and that from \mathbf{w} to \mathbf{h}_{out} . The singular values of the closed-loop systems shown in Fig. 5 clearly show that our design is capable of attenuating largely the effect of wind gust. In the worst situation, the wind gust effect (in terms of the worst case L_2 -gain) to \mathbf{h}_{out} can be reduced by more than 30%. This will be further verified this in the time-domain simulation to be given in Section 4.
2. *Locations of eigenvalues*: The eigenvalues of the closed-loop system for the hovering condition are depicted in Fig. 6. All of them are placed at the proper locations.
3. *Bandwidth of pitch and roll attitude responses*: The resulting frequency responses of pitch and roll attitudes give $\omega_{\text{BW}} = 3.11$ rad and $\tau_p = 0.038$ s for the pitch attitude response, and $\omega_{\text{BW}} = 3.22$ rad and $\tau_p = 0.0277$ s for the roll attitude response, respectively. In accordance with the standards set in [1], it is depicted in Fig. 7 that both channels achieve the top level performance.
4. *Coupling effect between roll and pitch responses*: To evaluate the performance in term of this specification, a step input signal with the amplitude of 0.15 is injected to δ_{lat} and δ_{lon} , respectively. The resulting ratio ($k_{\text{att,roll}}$ and $k_{\text{att,pitch}}$) are 0.092 and 0.052, which are both less than 0.25, the Level 1 performance requirement, as summarized in Fig. 7.
5. *Coupling effect from heave control to yaw response*: For the yaw and heave responses for a step input injected to δ_{col} with the amplitude of 0.02, we have obtained the ratios $k_{\text{yaw,1}}$ and $k_{\text{yaw,2}}$ are 0.142 and -0.141 , respectively. It is once again as summarized in Fig. 7 that the Level 1 performance is achieved.

6. *Crossover frequencies*: The crossover frequencies for the aileron and elevator channels are 2.51 rad/s and 2.31 rad/s, respectively. Both are lesser than the minimum requirement for the Level 1 performance, which is 10 rad/s.
7. *Disturbance rejection bandwidth for attitude control*: The frequency responses from attitude disturbances to attitude output show that the disturbance bandwidths for the roll and pitch

angles are 2.68 rad/s and 2.88 rad/s, respectively. Both of them exceed the Level 1 performance requirements (1 rad/s), as summarized in Fig. 7.

8. *Quickness of pitch, roll, and yaw responses*: The quickness ratios k_{qik} for the pitch, roll and yaw channels are respectively 2.82, 3.12, and 2.42, which satisfy the Level 1 performance requirement (see Fig. 7).
9. *Attitude hold for spike disturbance input*: Lastly, we examine the attitude hold response for a spike disturbance input injected in δ_{lon} or δ_{lat} . The amplitude and time span for the spike input are set as 0.8 and 0.1 s. The corresponding attitude responses results are depicted in Fig. 8. We note that the settling times t_{set} for the pitch and roll responses are 2.55 s and 2.91 s, respectively, which are less than 10 s, the Level 1 performance requirement.

In summary, the H_∞ control law that we have obtained for the hovering flight condition achieve the top level performance in all the categories under examination.

3.1.5. Control law for the full flight envelope

For testing the full-envelope flight on our unmanned system, HeLion, it is necessary to design a series of control laws for different flight conditions under examination, such as hovering, low and high speed flights. As mentioned before, for HeLion, we have selected 5 flight conditions which are corresponding to the forward flight speed $u = 0, 3, 6, 9$ and 12 m/s, respectively. The design of control laws and evaluation of their performances for other flight conditions follows the similar procedure as that for hovering. Instead of repeating the whole process over and over again, we have put the linearized models, the corresponding control laws, and associated performance evaluation results for all other flight conditions in the separate document for easy references. Interested readers are referred to [2] for more detailed information.

We adopt a simple gain scheduling scheme to realize the full-envelope flight. More specifically, for any intermediate status between two adjacent flight conditions, a linear interpolation is used to calculate the corresponding state feedback matrix F , the reference feedforward matrix G , and the trimmed values of the state and input variables. The reduced-order estimator given in (36) and (37) with its necessary associated matrices is employed for all flight conditions throughout our experiment. The effectiveness of such a gain scheduling method will be clearly shown in the

practical implementation of our control system design addressed later in Section 4.2.

3.2. Design of outer-loop control law

The outer-loop control law is designed to achieve the desired responses of the position and heading control in the NED frame. When it comes to design flight control systems for controlling the position and heading angle of the helicopter, it is common belief that it can be done by assuming all the channels are decoupled. In what follows, we first show that the outer-loop channels with the inner-loop being closed are indeed decoupled by further identifying their frequency responses on the actual platform. As such, we can safely treat each of the loops as a SISO system and design a control law for it one by one without worrying their coupling effects.

1. Open outer-loop dynamics: Shown in Fig. 9 is a detailed illustration of the open outer-loop system of the helicopter at hovering flight with its input variables, u_{nr} , v_{nr} , w_{nr} and r_r , being respectively velocity and yaw rate references generated by the flight task scheduling in the NED frame, whereas its output variables, p_x , p_y , p_z and ψ , being respectively the corresponding position and yaw angle also in the NED frame. We inject a series of chirp signals with frequencies ranging 0.05–3 rad/s and with appropriate amplitudes as well as with a time span of 30 s to each input channel of Fig. 9, in which the inner-loop dynamics is taken as the linearized model of (25) and the inner-loop controller is the H_∞ control law obtained in the previous subsection. Shown in Fig. 10 are the frequency responses we obtain by analyzing the resulting outputs through the usual system identification technique. It is clear from the result obtained that the coupling effects among the different channels in the outer loop are very minimal. The identified system models for

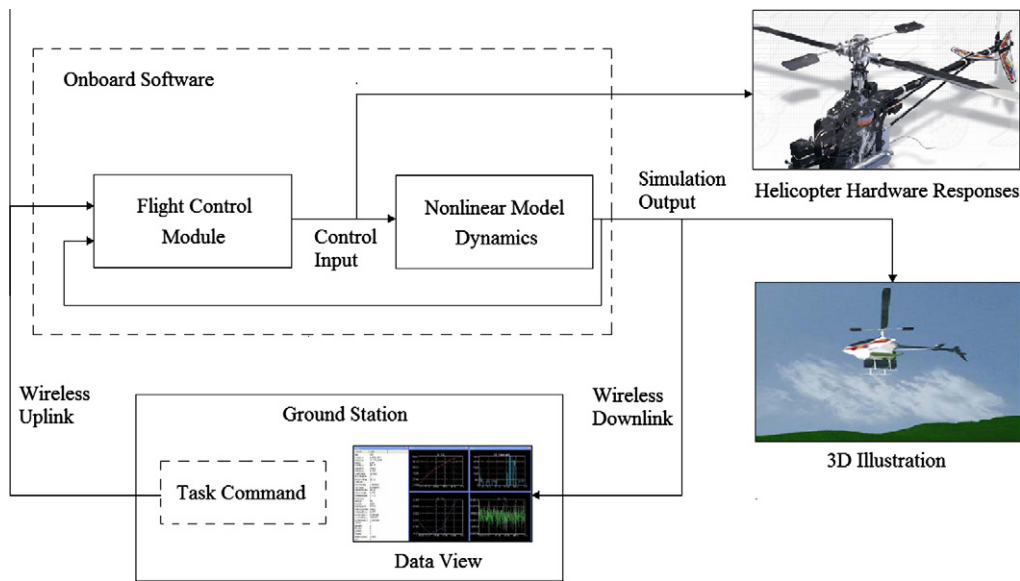


Fig. 11. Configuration of hardware-in-the-loop simulation experiment.

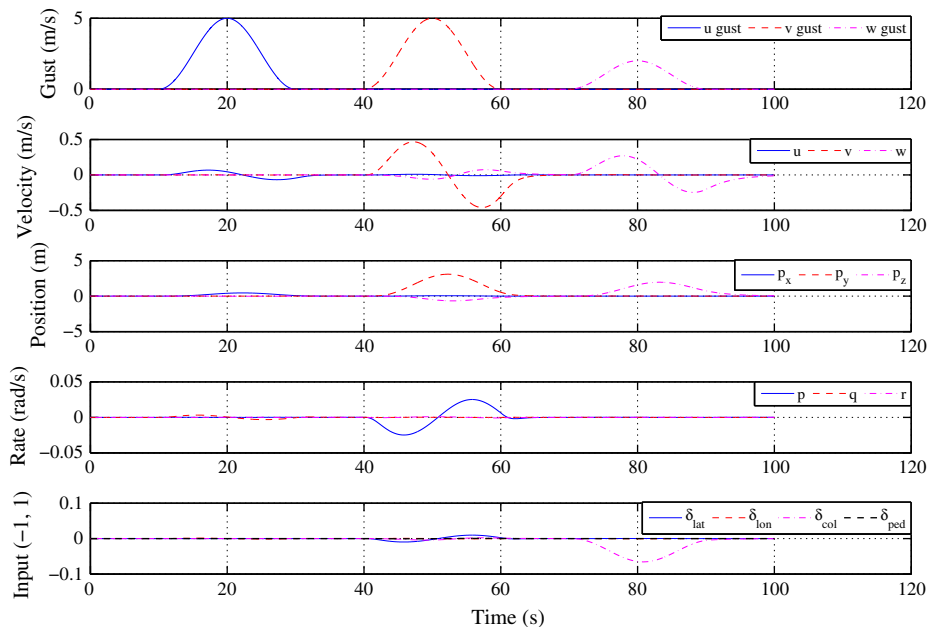


Fig. 12. Simulation results—wind gust attenuation of the overall closed-loop system at hovering.

each channel of the outer loop are given respectively as the following:

1. The transfer function between u_{nr} and p_x , i.e., along the x -axis, is given by

$$\mathbf{H}_x = \frac{1.7486}{s(s^2 + 1.8662s + 1.7277)} \quad (38)$$

2. The transfer function between v_{nr} and p_y , i.e., along the y -axis, is given by

$$\mathbf{H}_y = \frac{1.8541}{s(s^2 + 1.9883s + 1.8465)} \quad (39)$$

3. The transfer function between w_{nr} and p_z , i.e., in the heave direction, is given by

$$\mathbf{H}_z = \frac{1.2843}{s(s + 1.2843)} \quad (40)$$

4. The transfer function between r_r and ψ , i.e., the yaw channel, is given by

$$\mathbf{H}_{yaw} = \frac{33.0127s + 174.2323}{s(s^2 + 32.1901s + 173.1361)} \quad (41)$$

2. *Outer-loop controller design:* We propose in this section to design high performance outer-loop controllers using the CNF control technique, which has proven to be capable of yielding a very fast transient response with no or very minimal overshoot. The CNF control technique was first introduced by Lin et al. [19] to improve the tracking performance under state feedback laws for a class of second-order systems subject to actuator saturation. It has been fully developed in Chen et al. [7,8] to handle general systems with input constraints and with measurement feedback and applied to design high performance positioning mechanism for hard disk drive servo systems. The CNF control consists of a linear feedback law and a nonlinear feedback law without any switching element.

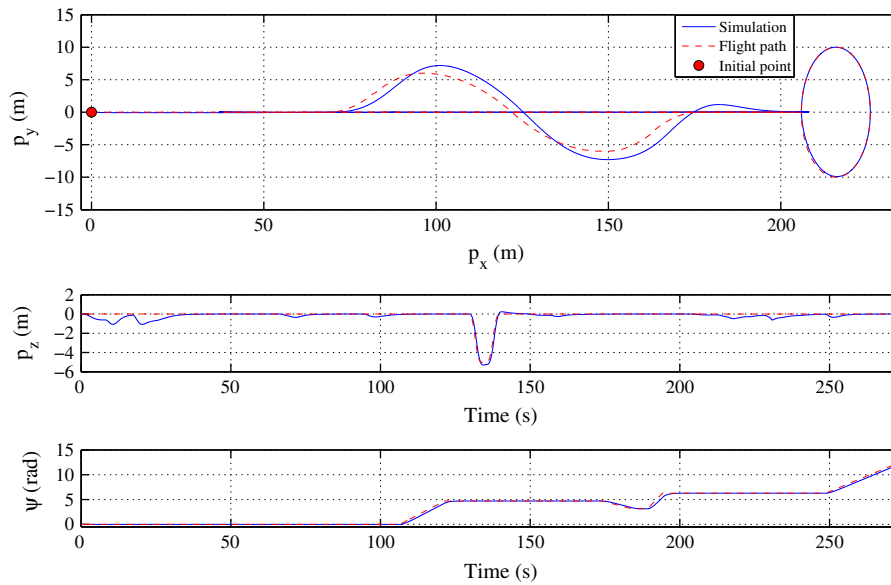


Fig. 13. Simulation results—the responses of the full-envelope flight of the overall unmanned system.

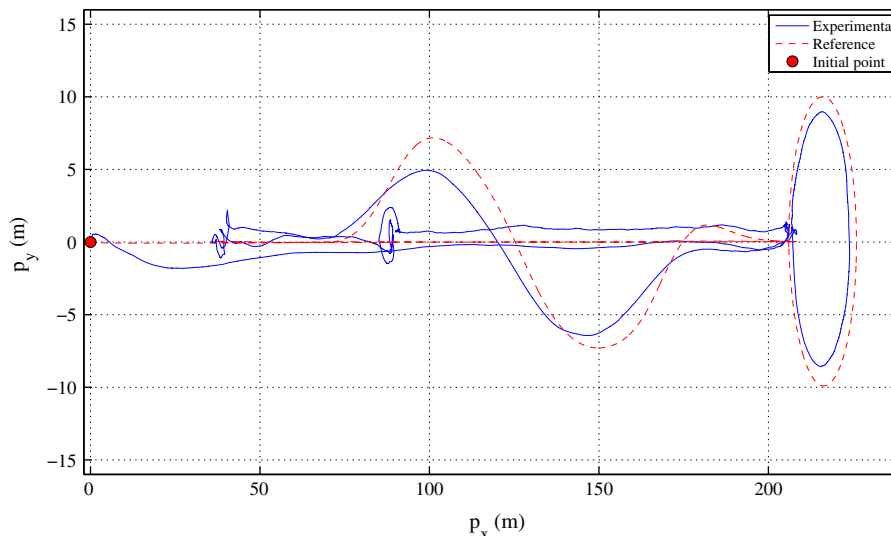


Fig. 14. Actual flight test—position (horizontal plane).

The linear feedback part is designed to yield a closed-loop system with a small damping ratio for a quick response, while at the same time not exceeding the actuator limits for the desired command input levels. The nonlinear feedback law is used to increase the damping ratio of the closed-loop system as the system output approaches the target reference to reduce the overshoot caused by the linear part. The design philosophy of the CNF technique is on reducing overshoot and speeding up its settling time of the overall control system.

To be more specific, we consider a linear continuous-time system Σ with an amplitude-constrained actuator characterized by

$$\begin{cases} \dot{\mathbf{x}}_{\text{CNF}} = A_{\text{CNF}} \mathbf{x}_{\text{CNF}} + B_{\text{CNF}} \text{sat}(\mathbf{u}_{\text{CNF}}), & \mathbf{x}_{\text{CNF}}(0) = \mathbf{x}_{\text{CNF},0} \\ \mathbf{y}_{\text{CNF}} = C_{\text{CNF}} \mathbf{x}_{\text{CNF}} \end{cases} \quad (42)$$

where $\mathbf{x}_{\text{CNF}} \in \mathbb{R}^n$, $\mathbf{u}_{\text{CNF}} \in \mathbb{R}$ and $\mathbf{y}_{\text{CNF}} \in \mathbb{R}$ are, respectively, the state, input and output of Σ . A_{CNF} , B_{CNF} and C_{CNF} are appropriate dimensional constant matrices, and $\text{sat}: \mathbb{R} \rightarrow \mathbb{R}$ represents the actuator saturation defined as

$$\text{sat}(\mathbf{u}_{\text{CNF}}) = \text{sgn}(\mathbf{u}_{\text{CNF}}) \min\{\mathbf{u}_{\text{CNF},\text{max}}, |\mathbf{u}_{\text{CNF}}|\} \quad (43)$$

with $\mathbf{u}_{\text{CNF},\text{max}}$ being the saturation level of the input. The following assumptions on the system matrices are required: (i) $(A_{\text{CNF}}, B_{\text{CNF}})$ is stabilizable, (ii) $(A_{\text{CNF}}, C_{\text{CNF}})$ is detectable, and (iii) $(A_{\text{CNF}}, B_{\text{CNF}}, C_{\text{CNF}})$ is invertible and has no invariant zeros at $s = 0$. The objective is to design a CNF control law that causes the output to track a high-amplitude step input rapidly without experiencing large overshoot and without the adverse actuator saturation effects. This is done through the design of a linear feedback law with a small closed loop damping ratio and a nonlinear feedback law through an appropriate Lyapunov function to cause the closed-loop system to be highly damped as the system output approaches the command input to reduce the overshoot.

In what follows, we recall from [7,8] the step-by-step procedure of the CNF control design with full order measurement feedback:

Step 1: Design a linear feedback law,

$$\mathbf{u}_{\text{CNF,L}} = F_{\text{CNF}} \mathbf{x}_{\text{CNF}} + G_{\text{CNF}} \mathbf{r}_{\text{CNF}} \quad (44)$$

where F_{CNF} is chosen such that (1) $A_{\text{CNF}} + B_{\text{CNF}} F_{\text{CNF}}$ is an asymptotically stable matrix, and (2) the closed-loop system $C_{\text{CNF}}(sI - A_{\text{CNF}} - B_{\text{CNF}} F_{\text{CNF}})^{-1} B_{\text{CNF}}$ has certain desired properties, e.g., having a small damping ratio. We note that such an F can be designed using methods such as the H_2 and H_∞ optimization approaches. Furthermore, G_{CNF} is a scalar and is given by

$$G_{\text{CNF}} = -[C_{\text{CNF}}(A_{\text{CNF}} + B_{\text{CNF}} F_{\text{CNF}})^{-1} B_{\text{CNF}}]^{-1} \quad (45)$$

and \mathbf{r}_{CNF} is a command input. Here we note that G_{CNF} is well defined because $A_{\text{CNF}} + B_{\text{CNF}} F_{\text{CNF}}$ is stable, and the triple $(A_{\text{CNF}}, B_{\text{CNF}}, C_{\text{CNF}})$ is invertible and has no invariant zeros at $s = 0$.

Step 2: Given a positive definite matrix $W_{\text{CNF}} \in \mathbb{R}^{n \times n}$, we solve the following Lyapunov equation:

$$(A_{\text{CNF}} + B_{\text{CNF}} F_{\text{CNF}})' P_{\text{CNF}} + P_{\text{CNF}} (A_{\text{CNF}} + B_{\text{CNF}} F_{\text{CNF}}) = -W_{\text{CNF}} \quad (46)$$

for $P_{\text{CNF}} > 0$. Such a solution is always existent as $A_{\text{CNF}} + B_{\text{CNF}} F_{\text{CNF}}$ is asymptotically stable. The nonlinear feedback portion of the CNF control law, $\mathbf{u}_{\text{CNF,N}}$, is given by

$$\mathbf{u}_{\text{CNF,N}} = \rho_{\text{CNF}}(\mathbf{e}_{\text{CNF}}) B_{\text{CNF}}' P_{\text{CNF}} (\mathbf{x}_{\text{CNF}} - \mathbf{x}_e) \quad (47)$$

where $\rho_{\text{CNF}}(\mathbf{e}_{\text{CNF}})$, with $\mathbf{e}_{\text{CNF}} = \mathbf{y}_{\text{CNF}} - \mathbf{r}_{\text{CNF}}$ being the tracking error, is a smooth and nonpositive function of $|\mathbf{e}_{\text{CNF}}|$. It is used to gradually change the system closed loop damping ratio to yield a better tracking performance. The choices of the design parameters, $\rho_{\text{CNF}}(\mathbf{e}_{\text{CNF}})$ and W_{CNF} , will be discussed later. Next, we define

$$G_e := -(A_{\text{CNF}} + B_{\text{CNF}} F_{\text{CNF}})^{-1} B_{\text{CNF}} G_{\text{CNF}} \quad (48)$$

If all the state variables of the system are available for feedback, the CNF control law is given by

$$\begin{aligned} \mathbf{u} &= \mathbf{u}_{\text{CNF,L}} + \mathbf{u}_{\text{CNF,N}} \\ &= F_{\text{CNF}} \mathbf{x}_{\text{CNF}} + G_{\text{CNF}} \mathbf{r}_{\text{CNF}} + \rho_{\text{CNF}}(\mathbf{e}_{\text{CNF}}) B_{\text{CNF}}' P_{\text{CNF}} (\mathbf{x}_{\text{CNF}} - G_e \mathbf{r}_{\text{CNF}}) \end{aligned} \quad (49)$$

Step 3: For the case when there is only a partial measurement available, the state feedback CNF control law of (49) should be replaced by the following measurement feedback controller:

$$\begin{cases} \dot{\mathbf{x}}_v = (A_{\text{CNF}} + K_{\text{CNF}} C_{\text{CNF}}) \mathbf{x}_v - K_{\text{CNF}} \mathbf{y}_{\text{CNF}} + B_{\text{CNF}} \text{Sat}(\mathbf{u}_{\text{CNF}}) \\ \mathbf{u}_{\text{CNF}} = F_{\text{CNF}} \mathbf{x}_v + G_{\text{CNF}} \mathbf{r}_{\text{CNF}} + \rho_{\text{CNF}}(\mathbf{e}_{\text{CNF}}) B_{\text{CNF}}' P_{\text{CNF}} (\mathbf{x}_v - G_e \mathbf{r}_{\text{CNF}}) \end{cases} \quad (50)$$

where K_{CNF} is the full order observer gain matrix such that $A_{\text{CNF,CMP}} = A_{\text{CNF}} + K_{\text{CNF}} C_{\text{CNF}}$.

The freedom to choose the function ρ_{CNF} in the CNF design is used to tune the control laws so as to improve the performance of the closed-loop system as the output, \mathbf{y}_{CNF} , approaches the set point, \mathbf{r}_{CNF} . Since the main purpose of adding the nonlinear part to the CNF controller is to shorten the settling time, or equivalently to contribute a significant value to the control input when the tracking error, \mathbf{e}_{CNF} , is small. The nonlinear part, in general, is set in action when the control signal is far away from its saturation level, and thus it does not cause the control input to hit its limits. The following nonlinear function is a good candidate used in the CNF Control Toolkit [9]:

$$\rho_{\text{CNF}}(\mathbf{e}_{\text{CNF}}) = -\beta_{\text{CNF}} \exp(-\alpha_{\text{CNF}} a_0 |\mathbf{e}_{\text{CNF}}|) \quad (51)$$

where α_{CNF} and β_{CNF} are tuning parameters to be adjusted to yield a desired performance, and $a_0 = 1/|\mathbf{e}_{\text{CNF}}(0)|$ if $\mathbf{e}_{\text{CNF}}(0) \neq 0$. For the case when $\mathbf{e}_{\text{CNF}}(0) = 0$, we select $a_0 = 1$.

With the help of the CNF Control Toolkit [9], we have successfully designed a set of nonlinear control laws for controlling the position of the UAV helicopter. More specifically, the CNF control laws for controlling both the x - and y -axis positions of the UAV are chosen to be identical and are given in the format of (50) together with $\rho_{\text{CNF}}(\mathbf{e}_{\text{CNF}})$ of (51) and

$$\begin{aligned} A_{\text{CNF,CMP}} &= \begin{bmatrix} -1.8418 & -1.6871 & -0.8824 \\ 1 & 0 & -4.6214 \\ 0 & 1 & -3.0372 \end{bmatrix}, \\ K_{\text{CNF}} &= -\begin{bmatrix} 0.5146 \\ 2.6954 \\ 1.7714 \end{bmatrix}, \quad B_{\text{CNF}} = \begin{bmatrix} 1 \\ 0 \\ 0 \end{bmatrix} \end{aligned} \quad (52)$$

$$\begin{aligned} F_{\text{CNF}} &= [-0.6299 \quad 0.0781 \quad -0.5865], \quad G_{\text{CNF}} = 0.3421, \\ F_n &= [1.0063 \quad 1.9872 \quad 0.8525] \end{aligned} \quad (53)$$

$$G_e = [0 \quad 0 \quad 0.5832]', \quad \beta_{\text{CNF}} = 2.2, \quad \alpha_{\text{CNF}} = 2.94 \quad (54)$$

We note that the control signal is limited to 2.5 m/s in both the x - and y -directions. For the heave direction positioning control, we have the following CNF control law:

$$A_{\text{CNF,CMP}} = \begin{bmatrix} -1.2843 & -3.4782 \\ 1 & -2.3037 \end{bmatrix}, \quad K_{\text{CNF}} = -\begin{bmatrix} 2.7083 \\ 1.7938 \end{bmatrix}, \quad (55)$$

$$B_{\text{CNF}} = \begin{bmatrix} 1 \\ 0 \end{bmatrix}$$

$$F_{\text{CNF}} = [0.3921 \quad -0.2301], \quad G_{\text{CNF}} = 0.1792, \quad F_n = [2.9961 \quad 2.1731] \quad (56)$$

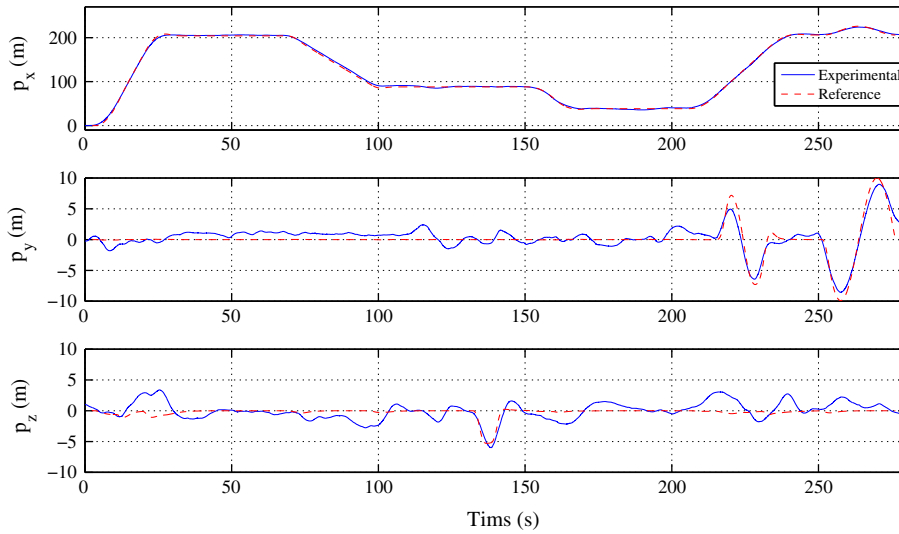


Fig. 15. Actual flight test—position.

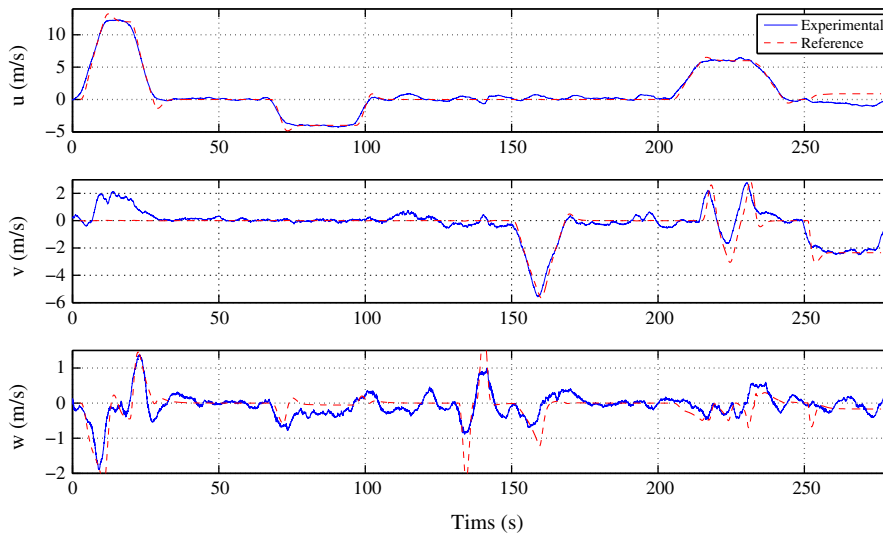


Fig. 16. Actual flight test—velocities.

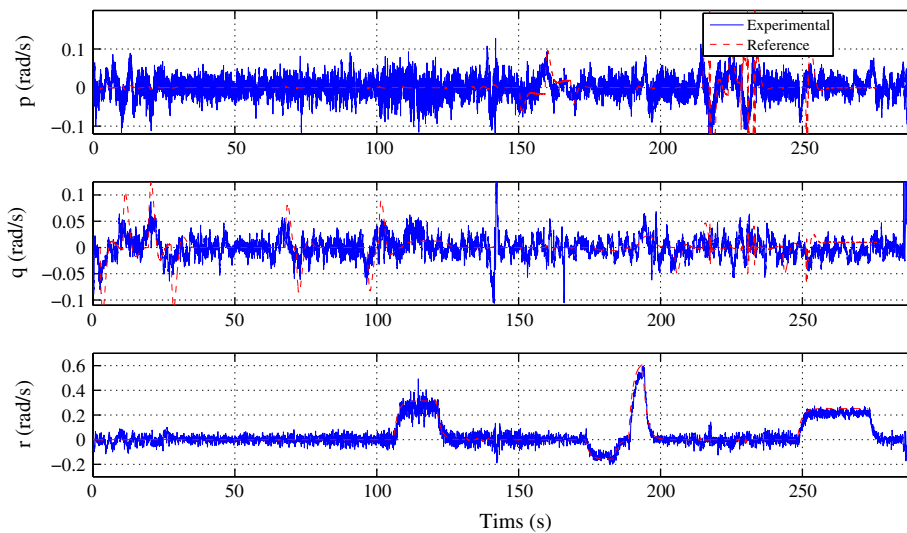


Fig. 17. Actual flight test—angular rates.

$$G_e = [0 \quad 0.77864]', \quad \beta_{CNF} = 1.5, \quad \alpha_{CNF} = 17.48 \quad (57)$$

We would like to note that we have added an additional term, i.e., $B_B^T P_{nc}$, where P_{nc} is the reference of the position vector in the NED frame, to the control inputs of the x -, y - and z -channels to compensate some steady-state errors. Finally, for the yaw channel, we use a simple proportional controller

$$r_r = k_\psi(\psi - \psi_c) \quad (58)$$

where ψ_c is the reference of the heading angle, and $k_\psi = -0.7$ is the proportional feedback gain. The above outer-loop controllers are used throughout all our simulation and implementation tests.

3.3. Flight scheduling configuration

In the flight-scheduling layer, we employ a predefined flight trajectory. More specifically, to effectively evaluate the practical performance of HeLion in the full flight envelope, we have selected one set of mission task elements (MTEs) defined in ADS-33D-PRF specification [1], and concatenated them with a custom defined mission (speed envelope test) to form the flight trajectory. The

simple descriptions of these MTEs are presented in Table 4. Interested readers are referred to [1] for detailed requirements on the desired performance of the listed MTEs. We should note that we have employed a simple but effective gain scheduling scheme based on the linear interpolation of the controller parameters associated with the respective flight conditions for the inner-loop control.

4. Simulation and actual flight test results

We present in this section both the simulation and actual implementation results for the flight control system obtained in the previous section. We would like to highlight that flight simulation, especially in the hardware-in-the-loop setting, is necessary and instrumental. It helps us avoiding many mistakes and errors before conducting actual flight tests.

4.1. Hardware-in-the-loop simulation result

We conduct a thorough evaluation of the performance of our flight control system through a hardware-in-the-loop simulation

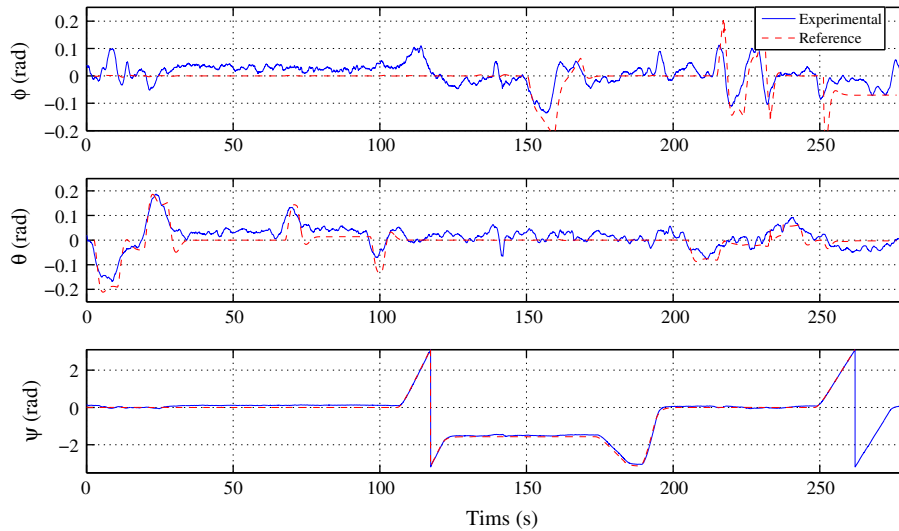


Fig. 18. Actual flight test—Euler angles.

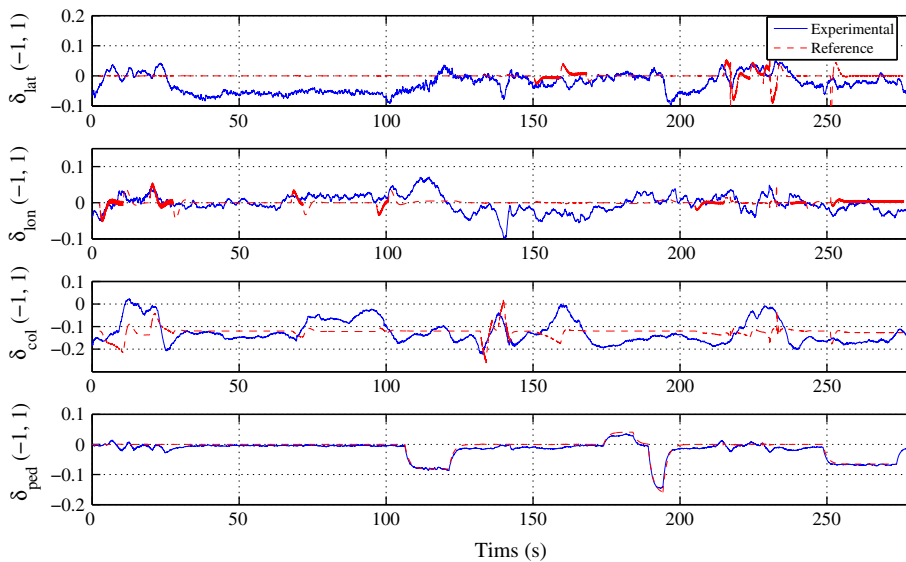


Fig. 19. Actual flight test—control inputs.

setup (see e.g., [5]). The general configuration of the simulation system is depicted in Fig. 11, in which a special computing unit has been used to simulate the nonlinear dynamical model of the UAV helicopter and further generate all the fifteen inflight state variables listed in Table 1. All other remaining components, such as the flight control module, wireless communications, and ground station execution, are identical to those used in actual experiments. The control input and the simulation output are injected into a 3D helicopter platform for straightforward observation. Interested readers are referred to [5] for more detailed information on our hardware-in-the-loop system.

A variety of simulation experiments have been conducted. Here we provide two representative examples. First, we show the wind gust attenuation of the overall closed-loop system for the hovering flight condition. The wind gust input and the corresponding output responses are shown in Fig. 12. In the simulation process, the 20-second-long '1-cos(.)'-style wind gust disturbance as suggested in [14], has been sequentially injected to the x -, y -, and z -directions of the body frame, with the peaking amplitude of 5, 5, and 2 m/s, respectively. The results clearly demonstrate that the wind gust effect has been effectively attenuated.

Fig. 13 shows the simulation result of the outer-loop responses of the overall closed-loop system, in which the ideal flight trajectory and the simulation are compared. It is clear that the position responses generated by the simulation process quite well matches the expected flight path, with the maximum deviation of 1–2 m. Regarding the heading angle, the matching is almost perfect. Such a simulation performance indicates that the flight control system we have designed is suitable for the actual implementation. It should be noted that in principle we can push for a faster response in the outer loop. In the actual flight experiment, however, it would require using a more accurate measurement setting.

4.2. Actual flight test result

The MTEs listed in Table 4 have been successfully executed in the actual experiment. The resulting responses, along with the reference signals, are compared and shown in Figs. 14–19. We would like to highlight that we intentionally conducted the flight test with the existence of strong wind gust (3–4 m/s in the horizontal plane, roughly measured by a handheld anemometer). Our test result shows that even with such wind gusts, the predefined flight trajectory can still be well maintained. In Figs. 14 and 15, we can observe the small deviation (about 2 m) of the actual trajectory from the reference path. Such inconsistency is mainly caused by the strong wing gusts disturbances.

In accordance with the requirements set for MTEs in [1], we can conclude that our flight control system is capable of achieving the desired performance for all the mission tasks.

5. Conclusion

We have presented in this work a complete flight control system design for a small-scale UAV helicopter. The simulation and actual flight tests show that our design is successful and capable of achieving the top level performance in accordance with the ADS-33D-PRF military rotorcraft standard. Interested readers can access the video clip of the actual flight test and the supplementary document of our work [2] through the web links available at <http://uav.ece.nus.edu.sg/>. The video is linked on our team's website under GALLERY in an item called "MTE-based full-envelope flight". Nonetheless, we believe that the overall control performance can be enhanced if there is a mean to obtain more accurate position

and yaw angle measurements. One possible solution is to use a differential GPS (DGPS). This might be crucial particularly for conducting flight formation and cooperative control of multiple unmanned systems. It is a subject currently under investigation by our UAV research group.

References

- [1] ADS-33D-PRF. Aeronautical design standard performance specification handling qualities requirements for military rotorcraft. US Army Aviation and Troop Command; 1996.
- [2] Cai G, Chen BM, Dong X, Lee TH. Supplementary document: Numerical results of flight dynamics model and control system design of Helion UAV. Technical Report, UAV Research Group, National University of Singapore; 2010. <<http://uav.ece.nus.edu.sg/>>.
- [3] Cai G, Chen BM, Lee TH. Design and implementation of robust automatic flight control system for a small-scale UAV helicopter. In: Proceedings of the 7th Asian control conference, Hong Kong, China; 2009. p. 691–7.
- [4] Cai G, Chen BM, Lee TH, Lum KY. Comprehensive nonlinear modeling of an unmanned-aerial-vehicle helicopter. In: Proceedings of the AIAA guidance, navigation, and control conference and exhibit, AIAA-2008-7414, Hawaii; 2008.
- [5] Cai G, Chen BM, Lee TH, Dong M. Design and implementation of a hardware-in-the-loop simulation system for small-scale UAV helicopters. Mechatronics 2009;19:1057–66.
- [6] Chen BM. Robust and H_∞ control. New York: Springer; 2000.
- [7] Chen BM, Lee TH, Peng K, Venkataramanan V. Composite nonlinear feedback control for linear systems with input saturation: theory and an application. IEEE Trans Automatic Control 2003;48:427–39.
- [8] Chen BM, Lee TH, Peng K, Venkataramanan V. Hard disk drive servo systems. 2nd ed. New York: Springer; 2006.
- [9] Cheng G, Chen BM, Peng K, Lee TH. A Matlab toolkit for composite nonlinear feedback control – improving transient response in tracking control. J Control Theory Appl 2010;8:271–9. <<http://uav.ece.nus.edu.sg/~bmcchen/>>.
- [10] CONDUIT user's guide. Moffett Field: US NASA Ames Research Center; 2009.
- [11] Enns R, Si J. Helicopter trimming and tracking control using direct neural dynamic programming. IEEE Trans Neural Netw 2003;14:929–39.
- [12] Flying-Cam Helicopter; April 2010. <www.flying-cam.com/products.php>.
- [13] Fujiwara D, Shin J, Hazawa K, Nonami K. H_∞ hovering and guidance control for autonomous small-scale unmanned helicopter. In: Proceedings of 2004 IEEE/RSJ international conference on intelligent robots and systems, Sendai, Japan; 2004. p. 2463–8.
- [14] Frost W, Turner RE. A discrete gust model for use in the design of wind energy conversion systems. J Appl Meteorol 1982;21:770C776.
- [15] Gadewadikar J, Lewis FL, Subbarao K, Chen BM. Structured H_∞ command and control loop design for unmanned helicopters. AIAA J Guidance, Control Dyn 2008;31:1093–102.
- [16] Heffley RK, Mnich MA. Minimum-complexity helicopter simulation math model. Technical Report NASA Contractor Report 177476, NASA; 1988.
- [17] Isidori A, Marconi L, Serrani A. Robust nonlinear motion control of a helicopter. IEEE Trans Automatic Control 2003;48:413–26.
- [18] Kim HJ, Shim DH, Sastry S. Flying robots: modeling, control and decision making. In: Proceedings of the 2002 IEEE international conference on robotics and automation, Washington, DC; 2002. p. 66–71.
- [19] Lin Z, Pachter M, Banda S. Toward improvement of tracking performance – nonlinear feedback for linear systems. Int J Control 1998;70:1–11.
- [20] Mettler B. Identification modeling and characteristics of miniature rotorcraft. Boston: Kluwer Academic Publisher; 2003.
- [21] Peng K, Cai G, Chen BM, Dong M, Lum KY, Lee TH. Design and implementation of an autonomous flight control law for a UAV helicopter. Automatica 2009;45:2333–8.
- [22] Roberts JM, Corke P, Buskey G. Low-cost flight control system for a small autonomous helicopter. In: Proceedings of the 2002 Australasia conference on robotics and automation, Auckland, New Zealand; 2002. p. 546–51.
- [23] SAE-AS94900. Aerospace – flight control systems – design, installation and test of piloted military aircraft, general specification for; July 2007.
- [24] Shim DH, Kim HJ, Sastry S. Decentralized nonlinear model predictive control of multiple flying robots. In: Proceedings of the 42nd IEEE conference on decision and control, Maui, Hawaii; 2003. p. 3621–6.
- [25] SR200 UAV; April 2010. <www.rotomotion.com/prd_UAV_SR200.html>.
- [26] Tischler MB, Colbourne JD, Morel MR, Biezad DJ. A multidisciplinary flight control development environment and its application to a helicopter. IEEE Control Syst Mag 1999;19:22–33.
- [27] Tischler MB, Colbourne JD, Morel MR, Biezad DJ, Levine WS, Moldoveanu V. CONDUIT—a new multidisciplinary integration environment for flight control development. Presented at the AIAA Guidance, Navigation, and Control Conference, AIAA-1997-3773, New Orleans; 1997.
- [28] Weilenmann MF, Christen U, Geering HP. Robust helicopter position control at hover. In: Proceedings of the 1994 American control conference, Baltimore, USA; 1999. p. 2491–5.